# HoloTrack: In-Situ Holographic Particle Tracking Velocimetry of Cloud Droplets

Birte Thiede[1,2], Freja Nordsiek[1], Yewon Kim[1], Eberhard Bodenschatz[1,2,3], and Gholamhossein Bagheri[1]

[1]Max Planck Institute for Dynamics and Self-Organization (MPIDS), Am Faßberg 17, 37077 Göttingen, Germany
[2]Faculty of Physics, University of Göttingen, Friedrich-Hund-Platz 1, 37077 Göttingen, Germany
[3]Laboratory of Atomic and Solid State Physics, Cornell University, 523 Clark Hall, Ithaca, NY 14853, USA

**Correspondence:** Gholamhossein Bagheri (gholamhossein.bagheri@ds.mpg.de)

**Abstract.** We present HoloTrack, a novel, fully autonomous measurement system designed to capture three-dimensional (3D) cloud droplet data and provide detailed insights into droplet dynamics, their spatial distribution and velocity. The HoloTrack system integrates a high-accuracy holographic imaging system with environmental sensors, including pitot tubes for airflow measurements, and a ~~motion-tracking~~ navigation system. Designed for deployment on airborne platforms like the CloudKite and hence having a compact and autonomous design, HoloTrack is also ideally suited for deployment in laboratory or ground-based environmental research. The system records up to 25 hologram pairs per second (50 holograms per seconds with the resolution of 65 megapixels), each of which provides two independent measurements of droplet position, size, and shape and measures individual droplet velocities~~in longitudinal and vertical direction. The~~. With laboratory tests we confirmed, that the holographic system reliably detects particles down to 10 µm, within a sample volume of 17 $cm^3$ (1.84 cm × 1.84 cm × 5 cm) of each hologram~~, which~~. For a recorded hologram pair with mean displacement of 0.5 cm caused by e.g. an inter-frame time of 500 µs and a mean velocity of 10 m/s, this results in 21.5 $cm^3$ ~~sampled~~ combined volume, where particle position and size is sampled and 12.3 $cm^3$ ~~sampled velocity for a mean displacement of 0.5 cm within hologram pairs~~overlapping volume where the two-frame particle velocimetry can be applied to resolve individual droplet velocities. Reliable sub-volumes for measuring droplets at different yaw angles, to account for the influence of the instrument body are further defined. The droplet velocity in longitudinal and vertical direction is measured with errors of less than ~~1.5% for mean velocities of 8-10~~ 0.07 m/s for inter-frame times of 500 µs. The transverse velocity is less accurate with errors in the range of 0.1-0.5 m/s, ~~but the~~ depending on the position of the particles in the sample volume. Nevertheless, the flexible timing allows ~~adjustment for larger mean displacements which increases accuracy if desired~~the adjustment to different displacements to optimize the overlapping volume and 3D velocity uncertainties according to the needs of the experiment. A series of ~~ground~~ laboratory tests and a maiden flight tests validated the system's capabilities, ~~confirming~~ characterizing the detection, robustness, automation and its ability to ~~accurately~~ measure droplet dynamics. HoloTrack's unique combination of holographic particle measurements including capturing their velocities makes it a powerful tool for advancing our understanding of cloud microphysics, including droplet spatial distribution, ~~coalescence~~collision-coalescence, entrainment, and turbulent mixing processes.

## 1 Introduction

Clouds have a significant influence on weather and climate and play a crucial role in the Earth's radiative energy budget. Cloud properties ~~are determined by the microphysics of clouds -~~ emerge from a complex interplay between microphysical processes, such as droplet size ~~, distribution~~distribution, and dynamics and ~~dynamics - which are closely linked to local thermodynamics and atmospheric turbulence (Shaw, 2003) . The evolution of droplet size distribution is intertwined with the underlying turbulent flow ,~~ large-scale cloud dynamics. Microphysics both respond to and influence the thermodynamic environment and turbulent motions within clouds (Shaw, 2003) with droplet size evolution closely linked to turbulent flow and the history of entrainment and mixing ~~in clouds~~ (Grabowski and Wang, 2013). Understanding these processes remains a challenge due to the multi-scale nature of clouds, from droplet-level physics to large-scale atmospheric dynamics (Bodenschatz et al., 2010)~~. Hence even in the most recent IPPC Sixth Assessment report clouds are stated to be still~~ which is why clouds remain the most uncertain climate feedback (Forster et al., 2021). ~~To resolve~~ Resolving individual cloud droplets ~~, which~~ is not possible via remote sensing (Grosvenor et al., 2018), ~~optical droplet~~ so optical probes are commonly deployed. Generally ~~the optical probes~~ these can be divided into two groups (see discussions about probes in e.g. Beals, 2013; Korolev et al., 2017): traditional probes measuring a single particle at a time, probing a quasi-1D volume and camera based measurements that sample droplets within large localized two-dimensional (~~(Schlenczek et al., 2025, e.g. PIV in MPCK$^+$)~~ (e.g. Particle Image Velocimetry, PIV, in M and (Bertens et al., 2021)) or with holography even three-dimensional cloud volumes with each sample~~(Beals, 2013; Korolev et al., 2017)~~ ~~.~~.

Holographic instruments have successfully measured cloud droplets in-situ for over 30 years (Brown, 1989), including current instruments like HOLODEC (Fugal and Shaw, 2009; Spuler and Fugal, 2011), HALOHolo (Schlenczek, 2018; O'Shea et al., 2016; Lloyd et al., 2020), HOLIMO (Henneberger et al., 2013; Ramelli et al., 2020) and the Advanced Max Planck CloudKite Instrument (MPCK$^+$) (Schlenczek et al., 2025; Thiede et al., 2025a). These ~~holographic measurements~~ systems allow comprehensive and more localized statistical analysis of cloud microphysical properties, such as concentration, local size distribution (Fugal and Shaw, 2009; Allwayin et al., 2024), and spatial characteristics like droplet clustering in full three dimensions (Borrmann et al., 1993; Larsen et al., 2018; Glienke et al., 2020; Thiede et al., 2025a) or analyze the cloud mixing behavior (Beals et al., 2015; Desai et al., 2021). ~~The intermittentor "patchy"~~ Recent studies confirm the intermittent, "patchy" nature of clouds ~~, although already discussed years ago (e.g. Jameson and Kostinski, 2001), is further confirmed by recent studies on size distribution (Allwayin et al., 2024) and droplet clustering by (Thiede et al., 2025a). Both studies find that cloud properties can vary significantly~~ (Jameson and Kostinski, 2001; Allwayin et al., 2024; Thiede et al., 2025a), with significant variations over small horizontal distances, ~~which underlines the utmost importance of these highly localized measurements only possible with imaging instruments having a large sample volume, which is an established feature of~~ highlighting the importance of large-volume, localized imaging provided by holography. Current holographic instruments ~~for measuring cloud droplets are capable of measuring the~~ measure 3D ~~position~~ droplet positions and cross-sectional ~~size and shape of~~ sizes for particles typically larger than ~~6-10~~6–10 µm within sample volumes of ~~up to around 10 cm~~the order of 10cm$^3$. Despite the described advantage of these measurements and recent achievements of holographic cloud droplet ~~measurement a key component~~

~~is still missing for a full description and hence understanding~~ measurements, a key aspect of cloud microphysics ~~: the~~ remains largely inaccessible: droplet dynamics.

~~While holographic~~ Holographic particle velocimetry has been successfully used in laboratory fluid dynamics contexts (Meng and Hussain, 1991; Hinsch, 2002; Tao et al., 2002; Hinsch and Herrmann, 2004; Meng et al., 2004; Svizher and Cohen, 2006, just to name a few), the high true-air-speed in airborne measurements and the constraints in camera pixel size and field of view to resolve the small cloud droplets, makes it a challenge for in-situ cloud measurements. Even ~~for the MPCK$^+$, which has the highest~~ the MPCK$^+$ instrument, with the highest airborne holographic sampling rate ~~of (~~75 Hz~~and a low true-air-speed )~~ on a tethered aerostat~~platform, subsequent holograms record~~ , captures entirely different sample volumes ~~and their is no overlap of field of view and hence no information about droplet dynamics~~can be assessed. ~~The MPCK$^+$, however,~~ in consecutive holograms, preventing assessment of droplet dynamics. MPCK$^+$ incorporates a 2D ~~Particle Image Velocimetry (PIV ) instrument to circumvent this bottleneck, which is the first application of an airborne PIV system , to provide information about the droplet dynamics. It only measures the droplet dynamics within a quasi-2D-laser~~ PIV system to measure droplet motion in a quasi-2D laser sheet (4 mm thick)~~without capturing droplet sizes~~, but it cannot capture individual droplet velocities and their size.

We have developed HoloTrack, the first holographic cloud droplet tracking velocimetry instrument that simultaneously measures droplet size and 3D velocity in a large, localized sample volume. By combining the low ~~true air velocity~~ true-air-speed of the Max Planck CloudKite ~~(MPCK) platform with recent advances in~~ platform with advanced camera technology and ~~a precise timingprotocol, we have developed the Holographic Droplet-Tracking instrument (HoloTrack ). This is the first airborne instrument capable of capturing hologram pair tracking of droplets in a large three-dimensional sample volume, providing droplet size and velocity data in a localized sample volume.~~ precise timing, HoloTrack captures hologram pairs with overlapping volumes, enabling droplet tracking in three dimensions. Figure 1 illustrates the principle: the system records a hologram pair ($H_1$ and $H_2$), and, based on the inter-frame time $\Delta t$ and mean true-air velocity $u$, droplets captured in the upstream part of $H_1$ are also captured downstream in $H_2$ (blue droplets in Figure 1). Matching droplets across the hologram pair allows computation of 3D velocities, though the $z$-component is associated with higher uncertainties. As holography also captures the cross-sectional size of particles, HoloTrack is not just limited to measuring droplets but also ideally suited for capturing non-spherical particles. In this paper, we present the design considerations and technical details involved in building HoloTrack. Through a test flight, wind tunnel droplet measurements, and our static test target ~~(CloudTarget) we comprehensively evaluate measurement~~ (i.e. the CloudTarget introduced in Thiede et al., 2025b) we comprehensively characterize detection, sizing, position and velocity uncertainties, outline potential improvements, and highlight HoloTrack's capabilities. ~~HoloTrack stands to be a significant contributor to future research, offering valuable insights into droplet formation, cloud microphysics, and turbulence.~~

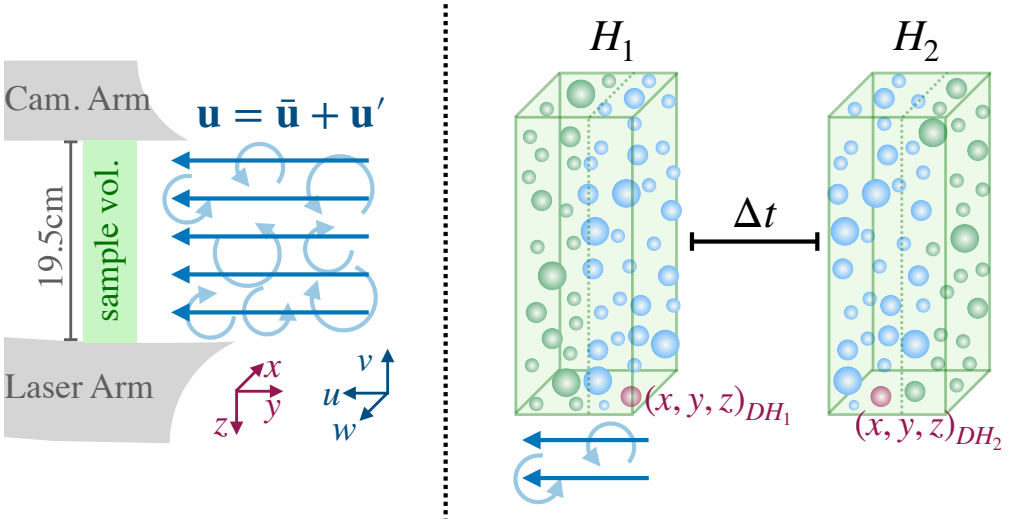


**Figure 1.** HoloTrack's design concept. Schematic showing HoloTrack's camera and laser arms and the sampling volume in droplet-laden turbulent flow (left), and a pair of hypothetical holograms of droplets, $H_1$ and $H_2$, with overlapping sample volumes (right). With a short enough inter-frame time $\Delta t$ the particles on the upstream part of sample $H_1$ are captured in the downstream part of $H_2$. By matching droplet $D$ between hologram $H_1$ and $H_2$ the 3D displacement and, hence, the 3D velocity can be calculated with $\mathbf{u} = (w,u,v) = (\bar{w}+w', \bar{u}+u', \bar{v}+v') = ((x,y,z)_{DH_1} - (x,y,z)_{DH_2})/(\Delta t)$, where an overbar denotes the mean (averaged) component and a prime denotes the fluctuating component.

## 2 Instrument Design

### 2.1 Mechanical Design

The HoloTrack planned design and the instrument that was finally manufactured are shown in Fig.2. With dimensions of 130 cm × 38 cm × 20 cm (excluding removable legs, battery holder and stabilizer fin), the HoloTrack instrument box maintains a moderate size, making it suitable for various laboratory setups and transportable within the Mobile Cloud Observatory for deployment on the CloudKite. The instrument consists of the main body that houses all key measurement logging and automation instruments, including two computers (see ~~section~~ Section 2.4) and the two upstream-oriented "arms" of the holographic system. This general design is inspired by previous holographic systems used for cloud droplet measurements such as HaloHolo and HoloDEC (Spuler and Fugal, 2011; Schlenczek, 2018). Termed ~~the~~th e"Laser Arm", one arm encapsulates the optics for laser beam alignment, expansion, and collimation. The second arm "Camera Arm" accommodates the camera that records the holograms without any lens.

HoloTrack was designed to have a stable laser beam-path system to avoid the need for realignment of the optics post-transportation or experiments. Therefore, both the laser and all optical components are mounted onto the single solid 2 cm thick base-plate with several screws to avoid any movement including vibrations. Aluminum was chosen as the material for the

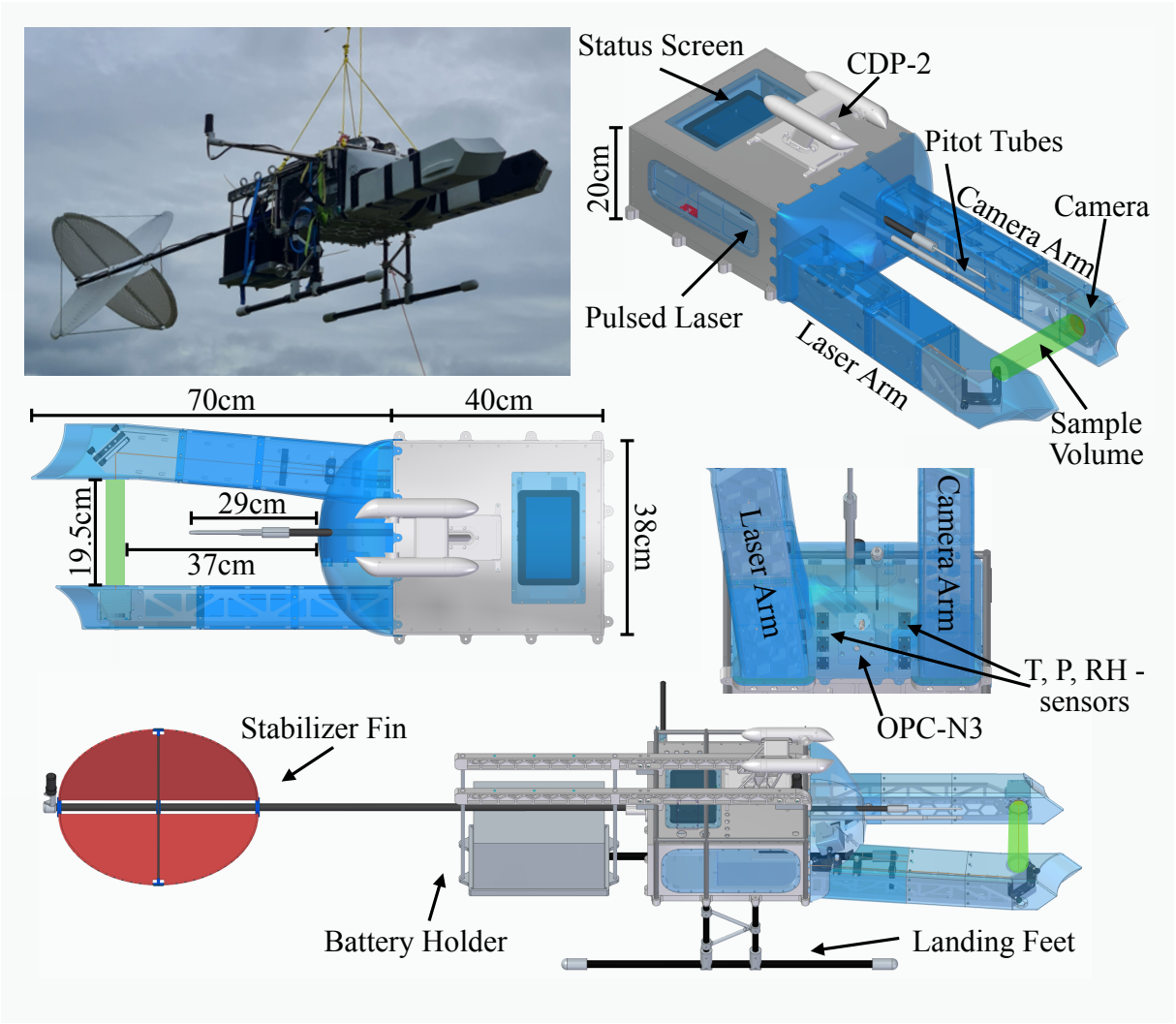


**Figure 2.** HoloTrack is an instrument box primarily designed for in-situ measurement of cloud droplet dynamics on the Max-Planck-CloudKites, while also being optimized for simple deployment in laboratory measurements. The top-right panel shows HoloTrack during its maiden flight aboard a CloudKite; the other panels present multi-view CAD visualizations of the instrument. The dimensions of the instrument are marked in the middle left panel, which is a top view of the instrument design plan. The instrument consists of the main box including electronics and devices for measurement control and acquisition. The arms contain the holographic system with camera and laser beam path. The measurement status of HoloTrack can be observed via a screen on top of the instrument. The holographic sample volume is shown in green. 1D and 3D pitot tubes are installed in the direction of the flow. In the cap small-scale sensors to measure environmental quantities and ~~OPC-N3~~ the optical particle counter are installed. For in-flight measurements a battery and a stabilizer fin can be fixed to the back of the instrument and landing feet ensure the sensitive parts of the instrument are always far from the ground in field measurements.

main instrument structure, which was optimized for weight by incorporating cutouts or a width reduction in honeycomb pattern in most structural components. The instrument can be easily handled and carried by two persons~~at most~~. The instrument box features side windows for the visual inspection of electronic connectors and status LEDs to enable error identification. A top window with integrated touchscreen allows operators to use the custom-made graphical measurement control software (written in Python Tkinter) and observe measurement status. Designed to withstand flight in precipitating clouds, the instrument box is constructed to be fully sealed and waterproof. The front of the instrument box as well as the arms of the holographic systems are designed to minimize the aerodynamic disturbance to the flow around them and, therefore, low aerodynamic disturbance in the sampling volume. This also ensures better alignment with the mean wind when attached to the CloudKite tethered balloon and minimal influence of the instrument body on the sample volume. The arm and front covers are 3D-printed and shown in blue in Figure 2. The hologram arms, long relative to the cross section of the instrument box, position the holographic sample volume at a large distance from the instrument body to minimize the impact of the bluff-body effect. The design of the tips of the holographic arms is inspired by the tips discussed in (Korolev et al., 2013) to avoid particle shattering. The holographic system's optical axis, which in our convention is the $z$-direction, is orientated horizontally, leading to a vertical orientation of the windows on the camera and laser arms, chosen to impede dust and water accumulation. For in-flight use HoloTrack is further equipped with a holder for the battery in the back and a stabilizer fin for mean-flow orientation as shown in the photo in Fig. 2. Acting as a heat sink, the base plate along with the honeycomb pattern effectively disperse heat into the surrounding flow. Nevertheless, the HoloTrack is equipped with two Peltier Elements for automatic temperature control for operations under more extreme temperatures.

### 2.2 Holographic Setup

In the design of the HoloTrack holographic instrument setup, we needed to consider various factors for accurate measurements of cloud droplets. Specifically, the smallest detectable droplets are desired to be around 6 µm, and typical expected velocities are on the order of 10 m/s. Particularly the detection of smaller droplets at higher depths within the holographic volume is limited by the cameras pixel size $d_{pixel}$, the field of view $N_x d_{pixel} \times N_y d_{pixel}$ in combination with the illumination wavelength $\lambda$. Therefore, the combination of illumination source and camera needs to be carefully chosen. Particles with a diameter smaller than two pixels can generally not be resolved using our standard hologram processing techniques with wavefront reconstruction via the Huygen-Fresnel kernel (Fugal et al., 2009). In addition to a small pixel size, the camera sensor should also have a large cross-sectional field of view. This feature is needed to resolve small droplets at larger depths, as the crucial particle information carried by diffraction patterns in holograms spreads over a large $x$-$y$ extent for small particles located farther from the camera sensor (detailed description in Fugal et al. (2009); Thiede et al. (2025b)).

HoloTracks holographic system, specifically, also demanded a camera with a high frame rate and flexible exposure timing options. A high frame rate is generally desired in in-situ holography to record the localized holographic samples at high spatial frequency. The XIMEA CB654MG-GP-X8G3 camera, with small pixel size of 3.2 $\mu$m and large field of view of $22.4 \times 29.9$ mm, has flexible timing and therefore allows for a short inter-frame time of sub-milliseconds within hologram pairs to allow particle tracking. The small pixel size also means that no lens is required for the camera, which simplifies the

design and significantly reduces the weight. The exterior-facing side of the camera window is at reconstructed $z = 2.5$ cm and the exterior-facing side of the laser window at $z = 22$ cm. The camera is operated at 8-bit.

For illumination a suitable coherent light source is needed. The laser pulse energy should be high enough to reach approximately 50% of the full well capacity $FWC$ in the camera after expansion and transmission through all optical components (see ~~section~~ Section 2.2.1) for optimal signal-to-noise ratio. The desired energy density can therefore be expressed as

$$e_d = \frac{0.5FWC}{qe(\lambda)} \frac{hc}{\lambda} d_{px}^2 \,, \tag{1}$$

where $qe(\lambda)$ is the quantum efficiency of the camera at the laser wavelength $\lambda$, $h$ is Plancks constant and $c$ the speed of light. The required pulse energy for the laser then depends on this desired energy density, the expansion of the beam up to a diameter of $d_{laser}$ at the camera sensor and the combined transmission of all optical components between laser head and camera $T_{all}$:

$$E_{pulse} = e_d T_{all} \pi \left( \frac{d_{laser}}{2} \right) . \tag{2}$$

To achieve an even illumination across the whole camera senors, the laser was expanded to $d_{laser} \approx 2 \times d_{camera}$, where $d_{camera}$ is the sensors diagonal (this is further discussed in ~~section~~ Section 2.2.1). We chose a green laser with 532 nm wavelength, the Explorer One XP (Newport Spectra-Physics). The laser offers flexible timing options including burst operation, a compact size and adequate pulse energy. While depth resolution decreases with wavelength, the chosen XIMEA CB654MG-GP-X8G3 camera has high quantum efficiency for 532 nm, hence the green laser being a good fit. The achieved $z$- and particle diameter-dependent detection is tested in Section 3.2. Lastly, the separation of the window in the laser arm and the camera arm window determines the effective sample volume dimension in $z$. Though ideally, a larger sample volume is always preferred, we settled for a separation of 19.5 cm. This is because the size of the smallest resolvable droplet decreases with an increase in $z$~~, and the total cross-sectional area of all obstacles in holography should not cover more than a few percent of the full cross-section.~~ . Additionally, the shadow density increases with larger $z$-component of the sample volume. According to empirical results by Royer (1974) hologram quality deteriorates for $SD > 1\%$ and a theoretical upper bound limit for which holography becomes unsuitable is given by Meng et al. (1993) with approximately 40% ($G = 1$ in Meng et al., 1993). With a 19.5 cm z-extent, ~~this limit is typically not reached in clouds~~the shadow density is $SD = \pi 19.5\text{cm}/4 \sum_i n_i d_i^2$ which would be 1%, 3%, 7% for 500 $\text{cm}^{-3}$ monodisperse droplets of 10,20,30 µm respectively. Hologram quality is therefore expected to only be strongly affected in conditions with exceptionally large number concentration and droplet sizes.

While the camera is able to reach frame rates up to 71 fps, we typically operate it at 50 fps i.e. 25 hologram pairs. At a nominal mean velocity of 10 m/s this ~~results in a sample volume sampled at~~ yields a three-dimensional sample every 40 cm horizontal distance ~~sampling the cloud a high horizontal spatial~~ resolving the cloud at sub-m resolution.

### 2.2.1 Laser Optics

We aimed to design a holographic system with collimated light to establish a rectangular sample volume. For this, on the laser side, the laser beam has to be expanded up to at least the sensor diameter $d_{laser} > d_{sensor} = 3.7$ cm to illuminate the full sample volume. To optimize for near-constant detection efficiency in the cross-section ($x$-$y$) even illumination of the sensor

is ideal. A straightforward solution is to expand the beam beyond the necessary diameter and utilize only the center of the Gaussian beam. In HoloTrack this expansion has to be achieved over a beam path of approximately 45 cm ~~as within the laser arm~~based on the current design setup. We accomplished the beam's expansion and collimation using a set of four aspheric lenses with focal lengths $f_1 = 8$ mm, $f_2 = 10$ mm, $f_3 = 32$ mm and $f_4 = 100$ mm as shown in Figure 3. The laser beam is emitted from the inside of the laser head with a small divergence angle. First, with an adjustable alignment mirror the beam is aligned into the center of the laser arm. The first three lenses amplify the divergence angle of the beam. The beam is spatially filtered with a 15 µm-pinhole, which is approximately 1.5 times the size of the beam waist, positioned in the first focus behind the $f_1 = 8$ mm aspheric lens. Towards the end of the laser arm, we placed the final fourth aspheric lens that collimates the beam when it has expanded to a theoretical diameter of approximately 8 cm. However, in practice, the aperture trims the beam to a final size of about 5 cm. After collimation, a mirror guides the beam into the sample volume.

Collimation was tested with different methods in the process of optimizing it and in CloudTarget evaluation we saw a negligible bias in the random position error of $z$ (see ~~section~~ Section 3.2). The beam intensity is adjusted with an absorbent neutral density filter to optimize the mean intensity in the holograms to about 50% of the well-depth. Given the timing constraints when operating the camera with minimal inter-frame times, the second frame of each hologram pair has a long exposure (see ~~section~~ Section 2.2.2 for details). Consequently, the collection of ambient sunlight by the camera needs to be limited. We accomplished this by using a bandpass filter with a 10 nm bandwidth centered at 532 nm and a liquid crystal shutter (FOS-AR, LC-TEC) in front of the camera sensor. The shutter, operable by a voltage signal, can be set to be open (with a transmission of 80% for polarized light, opening time 35 ms) or closed (0.02% transmission) within 150 µs (at 20°C, 350 µs at 0°C) and can be operated down to temperatures of $-10°$.

### 2.2.2 Timing

In the holographic system the timing of laser pulses, camera exposure and liquid crystal shutter is essential to successfully achieve short inter-frame times without measuring a high background intensity from the ambient sunlight. All the timings are controlled by a sequence generator developed by the in-house electronics department of the Max-Planck-Institute for Dynamics and Self-Organization (MPIDS). The sequence generator has 8 output channels, where the voltage (4 outputs with 5 V, 4 outputs with 24 V) can be controlled in µs-steps. With the outputs the laser pulse bursts are triggered, the camera exposure times are defined and triggered and the liquid crystal shutter is set into an open or closed state.

What we call inter-frame time is not exactly the time between the frames i.e. the time between camera exposures but the time between the two laser pulses recorded in holograms ~~A and B~~ $H_1$ and $H_1$ of a pair. The laser is running at a frequency $f_l$ and is emitting $n_P$ pulses per burst. The general idea to achieve accurate and short inter-frame times for tracking is that the first hologram ~~A~~ $H_1$ of each pair records the first laser pulse of each burst and the second frame records the $n_p$th pulse. The effective inter-frame time then is ~~$f_l\,(n_p - 1)\,\frac{1}{f_l}\,(n_p - 1)$~~. A lower limit for effective inter-frame time is the minimal time between the end of one frame and the start of the second frame, the frame overhead time, which is stated to be 28µs by the manufacturer Ximea. While minimal exposure time is technically 0.1 ms, the second exposure time needs to be equal or longer than the readout time of the first frame, which is related to the maximal frame rate $t_{rd} \approx \frac{1}{f_{max,cam}}$, where $f_{max,cam} = 71$Hz. Hence,

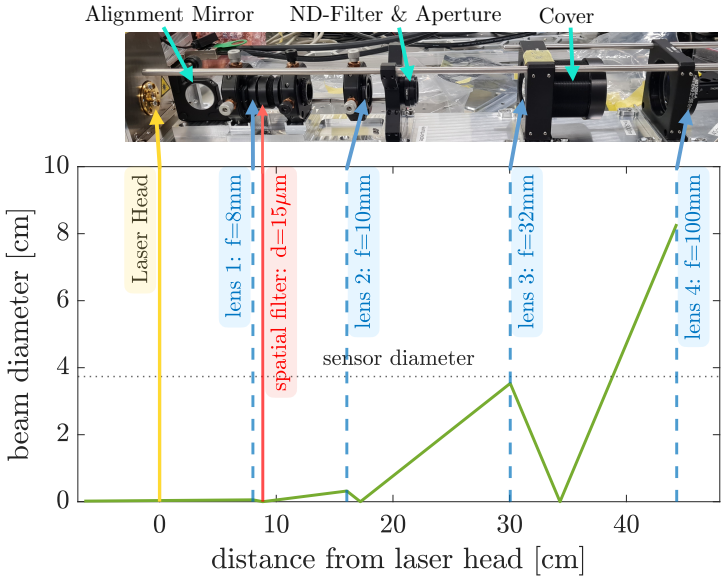


**Figure 3.** Beam path for laser beam alignment, expansion and collimation. In the top panel, the actual construction within the laser arm is shown. Optical elements are fixed in optical mounts, which are further stabilized (through the Thorlabs ~~systems~~Cage System). An adjustable mirror aligns the laser beam into the laser arm. The first two lenses for collimation are placed in x-y-translational stations, and the pinhole for spatial filtering is positioned at the beam waist in the focus of the first lens with the help of a x-y-z-translational stage. Behind the second lens, the beam intensity is reduced with a neutral density filter and the beam diameter is reduced with a circular aperture. The third lens is used to further expand the beam. The final lens collimates the beam and is therefore movable in z-direction. All holders are fixed with several screws into the base plate and/or stabilized by metal rods for optimized alignment. The bottom panel shows a simulation of the expected beam diameter as a function of z-distance. ~~This simulation code was used to optimize expansion~~ and collimation within the limits of available aspheric lenses, lens diameters and overall length of the beam path.

the first exposure ~~A~~ $H_1$ is set to be ~~$t_A = 0.1$~~$t_{H1} = 0.1$ ms but the second exposure ~~B~~ $H_2$ has to be ~~$t_B \approx 14$ ms~~$t_{H2} \approx t_{rd} - \Delta t$, where $\Delta t$ is the time between the two exposures. At a wavelength of 532 nm the ambient sunlight collected with the camera, even with the 10 nm bandpass filter installed, would increase the background intensity to a level above the actual signal from the laser. Therefore the liquid crystal shutter is timed to close after 0.1 ms of the second exposure.

The holographic system timing in HoloTrack was optimized for a mean flow speed of 10 m/s for all measurements shown in this paper, but it can be easily modified for 1 m/s to 100 m/s. For the timing protocol used here with inter-frame time of 500 µs, the laser frequency is set to 80 kHz and is configured in burst mode emitting bursts of each 41 pulses 25 times per second. The first exposure stops about 6µs after the first pulse and the second exposure starts 6µs before the 41st pulse, which ensures only a single laser pulse is recorded in each hologram. Therefore the effective inter-frame time is 500µs. The liquid crystal shutter is open for the whole duration of the laser pulse burst and closes ≈0.1 ms after last laser pulse. According to the manual of the laser the inaccuracy for the laser frequency and therefore for our effective inter-frame time is less that 0.1% at the 80 kHz used

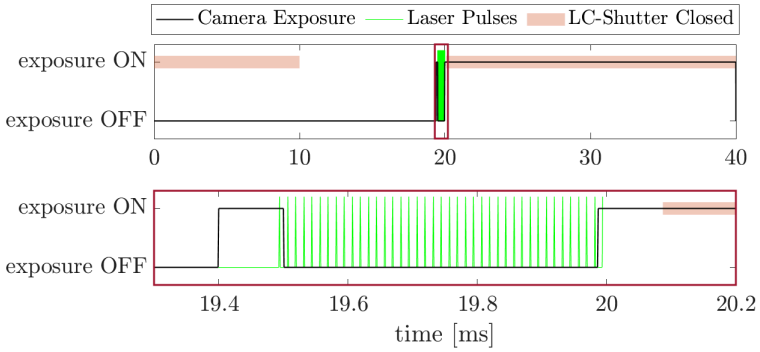


**Figure 4.** Timing diagram for recording one hologram pair with effective inter-frame time of 500µs. The first camera exposure is 100µs long and right before the camera shutter closes the first laser beam of the laser pulse burst is emitted. The burst consists of 41 pulses with a frequency of 80 kHz. Between the camera exposures 39 laser pulses are not recorded. The 41st laser pulse is right in the beginning of the long second exposure of the second hologram per pair. The longer exposure is limited to the read out time of the first hologram. The second exposure, is however effectively reduced to about 100µs with the help of a fast liquid crystal shutter.

in the described timing protocol to achieve 500µs. ~~Despite the simplicity of described timing, illustrated in the overview in Figure 4, the actual~~ The triggering signals emitted by the sequence generator have to take the laser, shutter and camera delays into account and the LC-shutter requires a specific signal pattern to be in the open or closed state. For different timing schemes, it is practical to adjust the number of laser pulses in the burst and keep the frequency constant at 80 kHz, since first-pulse suppression settings and the neutral density filters in the beam path would otherwise need to be changed to compensate for the varying pulse energies at different repetition rates. Therefore, the timing can be freely adjusted by 12.5 µs steps.

### 2.3 Measurement Instruments and Sensors

The HoloTrack instrument consists of several measurement systems, the main one certainly being the holographic particle tracking velocimetry system described above. Besides that, HoloTrack is equipped with two pitot Tubes for flow measurement. This includes a 1D pitot tube running at 100 Hz, where pressure is recorded and directly converted into velocities on the ADC (Air Data Computer by Simtec AG) and a 5-hole-pitot tube, running at 50 Hz, connected to the VectoDAQ which translates the pressured recorded in 5 angles into the three velocity components and flow angle of attacks.

The SBG Ellipse-N is an Inertial Navigation Unit (INU) providing information on orientation (roll, pitch, yaw), velocity, and position of HoloTrack through a combination of GPS and inertial data. This not only provides essential information about measurement location but also allows corrections of the measured velocities from the pitot tubes and the particle tracking velocimetry system for instrument motion. For redundancy a multi-band, centimeter-level GNSS receiver board (the simpleRTK2B ~~with U-Blox~~ by ArduSimple, integrating the u-blox ZED-F9P modules), is also installed on HoloTrack, ~~including 3 GPS antenna,~~ along with three GPS antennas. It is however currently not operational due to ~~usb-interface~~ USB-interface issues in the current version.

| Instrument Name | Manufacturer | Measured Quantities | Nom. Acquisition Rate [Hz] |
|---|---|---|---|
| Holographic System | in-house | individual 3D particle position (21.5 $cm^3$ per pair)<br>cross-section size and shape (21.5 $cm^3$ per pair)<br>2D particle velocity u,w (12.3 $cm^3$ per pair) | 25 (hologram pairs)<br>50 (individual holograms) |
| VectoDAQ | Vectoflow GmbH | 3D flow velocity $u$,$v$,$w$ | 50 |
| PSS8 ADC | Simtec AG | 1D flow velocity $u$ | 100 |
| SBG Ellipse-N | SBG Systems | 3D orientation, velocity, and GPS position | Acc. 390, Gyro. 133,<br>Magn. 22, GPS 5 |
| OPC-N3 | Alphasense | Particles, 0.35µm to 40 µm | 1 |
| SHT40 | Sensirion | Temperature, Relative Humidity (RH) | 15.3 |
| BMP390 | Bosch | Temperature, Pressure | 15.3 |
| TMP117 | Texas Instruments | Temperature | 15.3 |
| BME688 | Bosch | Temperature, RH,<br>absolute pressure, trace gases | 1 |
| **Future Instrumentation** | | | |
| simpleRTK2B with 3x<br>U-Blox ZED-F9P | ardusimple, U-Blox | GPS Data, 3D orientation | 10 |
| CDP-2 | Droplet Measurement Techniques | Particles in quasi 1D, 2 µm to 50 µm | continuous in 0.24 $mm^2$ cross section |

**Table 1.** Overview about the different measurement systems combined in HoloTrack. The main system is the holographic setup, supported by measurement of instrument position and movement as well as flow properties and measured quantities like temperature and relative humidity. The OPC-N3 and CDP-2 are additional particle sensors.

The OPC-N3 particle sensor can measure aerosols and small cloud droplets as a reference or potential trigger for the holographic system. HoloTrack is also designed to be equipped with the CDP2, which would provide reliable particle concentration and size distribution reference in a qausi-1D measurement. During the test flight and evaluation experiments shown below, no CDP2 was installed yet. In the cap of HoloTrack additional small-scale sensors (SHT40, BMP390, TMP117, BME688) are installed to measure quantities like temperature, pressure and relative humidity. See Table 1 for more details about these sensors.

### 2.4 Integration and Automation

HoloTrack is fully automated and can operate in two modes. In manual mode, an operator can start and stop holographic measurements using the graphical user interface on the mounted touchscreen. Alternatively, in trigger mode, measurements are initiated automatically based on altitude or particle concentration using devices such as the OPC-N3. By avoiding reliance on radio communications, which have caused problems in our previous instrument designs, the setup remains entirely autonomous.

The acquisition and automation system consists of two computers: the main computer controls the measurement status and logs data from all instruments listed in Table 1 except for holographic images. The camera of the holographic system is connected the ”holo-computer”, which logs only the holographic data. HoloTrack can be powered with a power supply in laboratory

settings or with a battery (see Figure 2 bottom) for in-flight measurements. The IP67 25.6 V, 50 Ah $LiFePO_4$ battery, which includes its own battery management system, provides sufficient capacity for several hours of flight. With four 1 TB hard disks a full hologram capture run can store approximately 60,000 holograms in about 20 minutes of continuous operation. As soon as HoloTrack is powered on the main computer boots and the measurement program with the graphical user interface is opened. With this, all measurement systems (described in ~~section~~ Section 2.3) except for holography are started and the recorded data is automatically logged on the main computer. We do currently see issues with connectivities of the sensors, likely cause by ground-loops, which leads to some intermittency in the data logging, leading to second-long gaps in the recorded data. Connection to sensors are checked continuously and once a missing sensor is back online, data acquisition continuous seamlessly. Due to laser safety considerations (see Section 2.5), as well as the system's high energy demands and substantial data production, the holographic system does not start automatically. Instead, it must be activated either manually through the graphical user interface or automatically triggered when operating in flight mode. This triggering is currently implemented to be caused by a certain barometric altitude. Before a flight on the CloudKite the cloud altitude can be determined by operators and set as a trigger limit. Since the OPC-N3 also measures particle count a triggering by this could also be implemented. The holographic system is turned on in 3 levels *Ready*, *Arm* and *Acquisition*. These levels can be selected manually or by a trigger and exist to prevent waiting times for start of acquisition due to minutes-long boot times of the holographic computer or temperature stabilizing time of the laser head. In the *Ready* state the camera and the holo-computer for hologram acquisition are turned on. The holographic capturing code starts up automatically on the holo-computer and as soon as the main computer can communicate with the holo-computer, the holographic state is *Ready*. The hologram acquisition code on the holographic computer would now save any incoming frames. For *Arm* the laser is turned on and is trying to reach a stable temperature. To reach the final *Acquisition*-state, where holograms are actually recorded, all interlocks are closed and the sequence generator is powered to send triggering signals to the laser, the camera and the liquid crystal shutter to follow the timing protocol described in ~~section~~ Section 2.2.2. If only a brief interruption from hologram acquisition is planned a switch from *Acquisition* to *Arm* and back is more time- and energy efficient than turning on and off the full system.

The automation was rigorously tested in laboratory conditions as well as in real flight conditions on a test flight~~during the IMPACT campaign in May-June 2024, at Pallas northern Finland, ~~, as described in ~~section~~ Section 3.1. The holographic system was successfully triggered by barometric altitude measurement and the holographic system automatically shut off after the disk was full. This automatic shutoff is essential to make handling of the instrument during landing easier and removes any danger from scattered laser light.

### 2.5 Laser Safety Considerations

The Laser used in the holographic system of the HoloTrack has laser Class IV. However, most of the pulse energy is absorbed within the optical system. For safety calculation we assumed a transmission of <32% (ND-filter with ND of 0.5 is used, other optics add even less transmission) of the <200µJ (typically 65µJ) beam and an expansion of the beam to a circular area with diameter 5 cm (actual expansion larger see ~~section~~ Section 2.2.1). Even with these upper bound assumptions, laser safety is guaranteed if operators do not come closer than 36 cm to the sample volume and ~~are~~ do not look directly into the laser beam

or direct reflections.

For safety reasons HoloTrack is equipped with an external laser key on the top of the box, only if the key is in and turned the laser can emit. There is an additional interlock closed by a relay controlled by our HoloTrack control program, closed only when holographic measurements are started. Additionally, a powerful LED, visible from several hundred meters even in daylight, flashes whenever the laser is emitting.

## 3 Performance Evaluation

For evaluation, we carried out three distinct experiments to verify and quantify HoloTrack's performance. ~~During~~ Firstly, during the IMPACT campaign ~~,~~ ("In-situ Measurement of Particles, Atmosphere, Cloud and Turbulence" May-June 2025, Pallas Finland), HoloTrack had its maiden flight, successfully collecting various datasets, including holograms~~, as planned~~. Although a broken pinhole in the holographic optical system rendered the collected holograms too bright to be usable, the test flight still demonstrated HoloTrack's ability to operate effectively under flight conditions. Additionally, we analyzed the relative motion of HoloTrack when attached to the CloudKite. ~~The~~ These results of the test flight are shown in ~~section 3.1.~~Section 3.1.

After replacement of the pinhole~~further evaluation tests were carried out in laboratory settings. Two~~ , evaluation of the holographic system was carried with experiments under laboratory conditions. Secondly, wo vital performance indicators, recall and accuracy of inter-particle distance measurement in the holograms, were assessed through CloudTarget test holograms, presented in ~~section~~ Section 3.2. Inter-particle distance accuracy directly relates to the accuracy of velocity measurement which makes this assessment crucial. Lastly, with wind tunnel experiments the accuracy of the holographic particle tracking velocimetry and the effect of a non-zero yaw angle on the holographic measurment is assessed 3.3. The holograms recorded in the different experiments were processed using the methods described in (Thiede et al., 2025b), developed originally for the MPCK$^+$holographic system. This includes background removal and object classification with the Convolutional Neural Network (CNN) with an optimal Particle Classification Threshold of 0.3. The reconstructed $z$-positions between 2.5 and 22 cm are within the sample volume.

### 3.1 Flight Test

#### 3.1.1 ~~System~~ Test Configuration and Automation Performance

During the IMPACT campaign~~in May-June 2024 in the subarctic region of Finnish Lapland~~, a test flight with HoloTrack on the Max Planck CloudKite (MPCK) platform was performed. The test flight lasted about 70 minutes in total. As explained above, the pinhole used for spatial filtering of the laser beam was broken during the flight and in the campaign only the single short test flight was possible for HoloTrack. Hence, ~~we can~~ for this test flight we could not evaluate in-situ holograms. We however tested the in-flight automated control for starting the hologram acquisition, hologram acquisition itself, data collection with other sensors and the motion of HoloTrack in-flight.

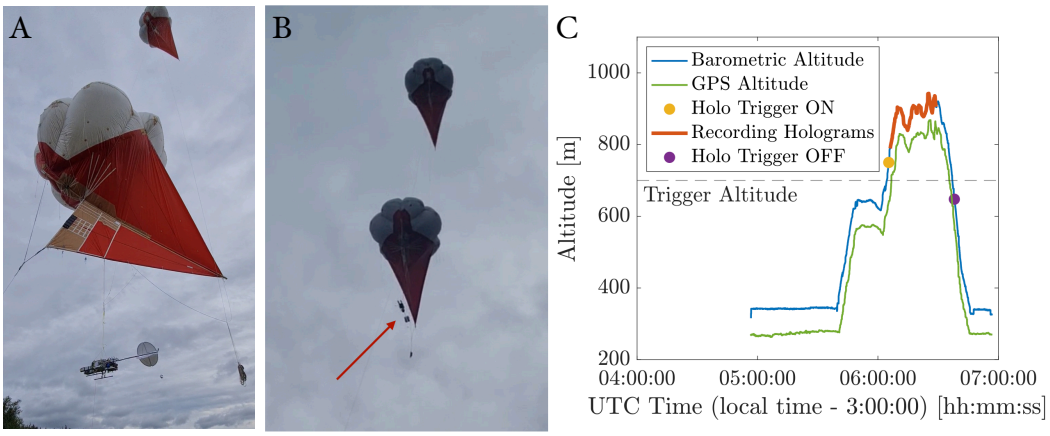


**Figure 5.** ~~Left~~A: Mounting on HoloTrack on the MPCK platform with a 3 m line from the keel. B: HoloTrack in flight on the MPCK platform. The red arrow shows the HoloTrack hanging ~~5~~6 m below the lower Helikite of the MPCK platform. ~~Right~~C: Overview about test flight. The holographic system was running in altitude trigger mode with a limit of 700m of barometric altitude. The yellow point indicates when the control system is turning the holographic system on. Shortly after the holographic system starts acquiring images for about 20 minutes until the disks are full (4TB at 25 hologram pairs per second). The system successfully shut off when altitude was below the limit again.

Firstly, the structural design of HoloTrack withheld the flight conditions without any problems. After the test flight no problems could be identified and the optical components were still aligned. No humidity reached the inside of the sealed instrument box. Moreover, the handling of HoloTrack during take off and landing was easy due to design considerations such as the landing feet.

Figure 5 B shows a photograph of the combination of two Helikites flying the HoloTrack instrument into the clouds. ~~We also~~ For the maiden flight, HoloTrack was attached with a line about 3 m below the keel of the lower Helikite, which results in a distance of 6 m to the balloon for ease of operation (see Figure 5 A). The hanging point is approximately 6.5 m downstream of the balloon edge. Hence, the wake does not reach HoloTrack as long as the pitch angle of attack is smaller than approximately 45°. As demonstrated in Figure 6, in the test flight the standard deviation of the pitch angle was only 10° with a mean of 0°. While even in this configuration the effect of the balloon is minimal, in future flights HoloTrack can be hung on a line directly from the tether at arbitrary distances below the balloon e.g. 10 m to 1000 m (as shown for WinDarts in Chávez-Medina et al., 2025). We show a general overview of the test flight including the altitude profile of measured barometric altitude and GPS altitude in Figure 5 C. The offset between the barometric and GPS altitude we show is due to the assumption of an average ground level static pressure in our real-time calculation of the barometric altitude from the measured pressure. This barometric altitude was used to trigger the holographic system as explained in ~~section~~ Section 2.4. The limit altitude for triggering was set to 700 m. Less than one minute after reaching that altitude the holographic system is triggered and another 2 minutes later holograms were recorded. The delay in triggering is intentionally set to avoid quick switching from ON to OFF trigger states when height oscillates around the trigger limit altitude. The delay between trigger and acquisition is due to the components of the holo-

graphic system having a fixed order in which they are turned on to ensure correct operation. Additionally, the laser needs time to stabilize the laser head temperature. The hologram acquisition stops after 20 minutes of hologram recording at a constant rate of 25 hologram pairs per second. When altitude is lowered below the Trigger Altitude all components of the holographic system were automatically turned off ensuring a safe landing. In terms of automation, the test flight went exactly as planned.

### 3.1.2 Instrument In-Flight Stability

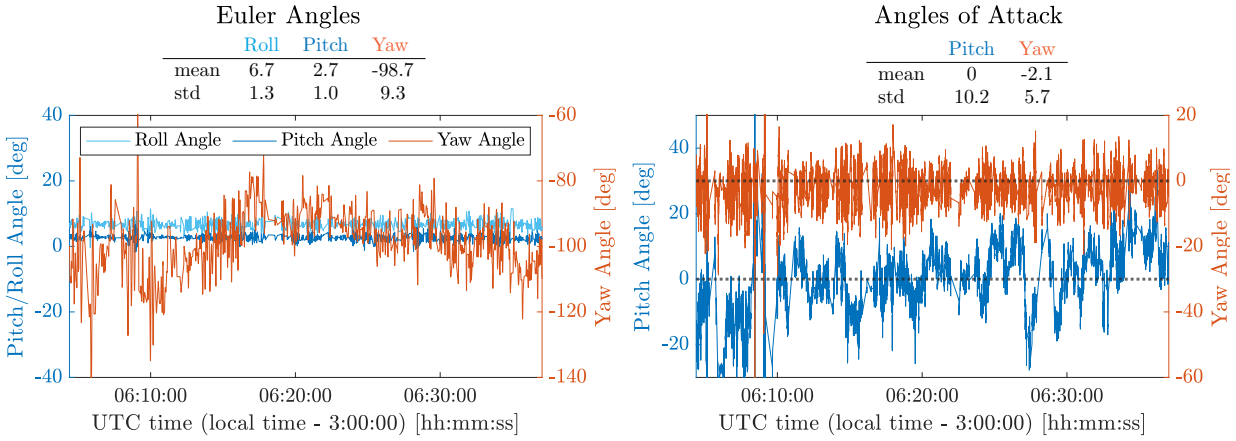


**Figure 6.** From the SBG the motion in terms of Euler Angles of the HoloTrack during flight are analyzed. Here, we show the motion for barometric altitude >700 m, which is the altitude chosen for holographic measurements in the test flight. The mean yaw angle changes with altitude and the fluctuations are on the order of 10°. From the 3D-velocity measurements the flow angles reveal that HoloTrack aligns well with the mean flow (mean yaw angle close to 0). Pitch angle shows influence of relative vertical velocity due to upward/ downward motion.

Another important parameter to be tested here is the motion of HoloTrack mounted by hanging on a passive tethered aerostat. The instrument layout was designed such that the instrument aligns with the mean wind, i.e. the hologram arms point upwind. Ideally, the instrument should be stable in the other directions, pitch and roll angles should be constant. The motion of the instrument in terms of Euler Angles was measured with the SBG-Ellipse INU and shown on the left in Figure 6 for the section of the flight where the holographic trigger was ON i.e. the barometric altitude was above 700 m.

Roll and Pitch Angle have slight mean offsets from 0° that do not affect measurements. The standard deviations of around 1° and the time series reveal little to no motion in roll and pitch direction. Although the inertial navigation unit (INU) indicates higher yaw fluctuation and a shifting mean, which reflects the orientation of HoloTrack's holographic arm relative to magnetic north, the more relevant measure for aerodynamic disturbances is the flow yaw angle (angle of attack) from the 5-hole pitot. As shown in Figure 6-right, this flow yaw angle of attack remains near ~~0°irc~~ 0° and thus HoloTrack's y-axis aligns closely with the mean flow. The discrepancy between the INU yaw and 5-hole pitot yaw arises from changes in the mean flow direction with altitude. Overall, HoloTrack maintains a stable angle of attack, with only moderate yaw-angle-of-attack fluctuations of

about 6°.

The pitch angle of attack is directly affected by relative vertical velocities caused by up- and downward movements of HoloTrack (negative/positive pitch angle for upward/downward motion) and would need to be corrected for the instrument motion, if vertical flow is to be analyzed. Of course, the angles observed here are specific to this flight and the motion of the instrument can differ in other conditions such as higher turbulence. They do, however, give a first indication that HoloTrack tends to align with the mean flow, which is optimal for the holographic measurement as the flow in the sample volume would be least affected by the arms. The motion of HoloTrack are also small enough such that a perturbation of the flow from the instrument motion is negligible. The blockage and flow disturbing effects from the arms depending on the yaw angle, are however not negligible, and are further analyzed with wind tunnel experiments in ~~section~~ Section 3.3.3.

### 3.1.3 Dissipation Rate Estimation from pitot Tube Measurements

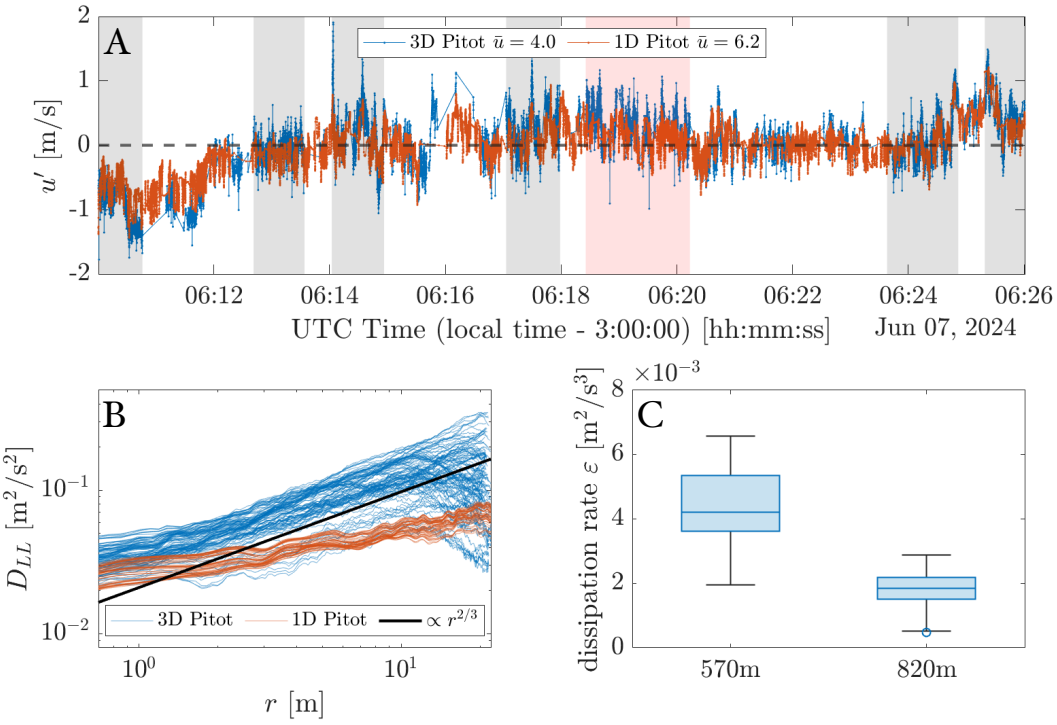


**Figure 7.** ~~Top~~**A**: Velocity fluctuation measured with 1D (100 Hz, 8-point averaging effectively 12.5 Hz) and 3D pitot tubes (50 Hz) in a region of ≈ 820 m altitude show overall agreement. Sections with continuous measurements are marked with shading. ~~Left~~**B**: The second order longitudinal structure function only reveals $r^{2/3}$-scaling in the inertial sub-range for the measurements with 3D pitot tube. ~~Right~~**C**: From the structure function the dissipation rate $\varepsilon$ was determined for the shaded red region shown in ~~the top~~ panel **A** (820 m) and another region at lower altitude (570 m).

To evaluate the possibility to capture turbulence properties not just from the holographic droplet measurements but also from the pitot tubes, next we look at the velocity fluctuations $u'$ in head-on or longitudinal direction, which both the 1D and the 3D pitot tube captured. A time series of the velocity fluctuations from both pitot tubes are shown in ~~the top panel~~ panel **A** of Figure 7 for a near-constant altitude section (820 $\pm$ 7 m) where instrument motion can be neglected for now. On a first glance the fluctuations seem to agree, the fluctuations observed with the 1D pitot tube are however smaller even though it operates at twice the frequency of the 3D pitot tube (100 Hz compared to 50 Hz). In the 1D pitot tube data recorder the default 8-point-filtering was still set, hence the velocity is averaged over 8 data points and turbulence is mostly filtered out. As discussed above, during the flight the recorded data from the non-holographic sensors were not continuous, which is further discussed in the discussion ~~section~~ Section 4. For further analysis, we therefore selected a continuous sub-section where the data from both pitot tubes was logged continuously at the expected frequency. This section is marked with red shading in ~~the top panel~~ panel **A**, and grey shading show continuous operation of the 3D pitot tube. From the velocity fluctuation in the marked section, the longitudinal 2nd order structure function (assuming Taylor's frozen flow)

$$D_{LL}(r) = \langle [u'(t + r/\bar{u}) - u'(t)]^2 \rangle \tag{3}$$

is calculated and shown in ~~the bottom left panel~~ panel **B** of Figure 7 for both pitot tubes. According to Kolmogorov's 1941 theory of turbulence $D_{LL} \propto r^{2/3}$ in the inertial sub-range, which we do observe for the 3D pitot tube data but not for the 1D pitot tube~~caused likely with~~. This is likely caused by the default 8-point-averaging filtering that was still set for 1D pitot tube recorder, effectively averaging out turbulence signal. From the 2nd order structure function $D_{LL}(r)$ in the inertial sub-range of the 3D pitot tube velocity fluctuation data the dissipation rate can the be calculated with

$$\varepsilon = \left( \frac{D_{LL}(r)}{2} \right)^{3/2} r. \tag{4}$$

as explained in detail in (Schröder, 2023). For the red shaded section at altitude 820 m shown in ~~the top panel~~ panel **A**, the dissipation rate is on the order of 0.002 m$^2$/s$^{~~2~~ 3}$ for a second analyzed section at lower altitude of 570 m we find a higher dissipation rate of 0.004 m$^2$/s$^{~~2~~3}$. We expect to be able to estimate the dissipation rate based on the 1D pitot tube data, if the default 8-point filtering is turned off and more importantly, from the holographic droplet velocities of small droplets in a single hologram (if droplet number concentration is sufficiently large). Therefore, with HoloTrack we will have three independent measurements of turbulence statistics, such as the dissipation rate and with the holographic measurement offering the most localized one.

Even the larger dissipation found here of approximately $\varepsilon$ =0.004 m$^2$/s$^2$ would result in Stokes numbers of ~~0.003 and 0.08~~ 0.005 and 0.13 ($St = \frac{\tau_p}{\tau_K}$, where $\tau_p = \frac{\rho_d d^2}{18 \mu_{air}}$ is the particle response time and $\tau_K = \sqrt{\nu_{air}/\varepsilon}$ is the Kolgomorov timescale) and settling parameters of 0.2 and 5 ($Sv = \frac{w_s}{u_K}$ where $w_s = \frac{(\rho_d - \rho_{air} g d^2)}{18 \mu_{air}}$ is the settling velocity and $u_K = (\nu_{air} \varepsilon)$ the Kolmogorov velocity scale) for 10 µm and 50 µm diameter droplets respectively. In these conditions, we would expect even large cloud droplets to ~~follow the flow~~not have significant inertial effects (low St) but gravitational effects would be measurable. This deviation of droplets from the mean flow due to gravitational settling could be captured by HoloTrack. In more turbulent conditions or for even larger droplets, the strength of HoloTrack would be to observe the decoupling of larger droplets from the

flow due to inertial effects ~~quantified by a large Stokes number~~as well.

### 3.2 Holography Performance Evaluation and Characterization: Static CloudTarget Tests

To assess detection efficiency of the HoloTrack holographic system we performed laboratory measurements with the CloudTarget (see Thiede et al., 2025b, for more details). The CloudTarget consists of chrome photomasks with a pattern of opaque circular disks with diameters between 4 and 70 µm. The diffraction pattern of a water droplet can be approximated with the diffraction pattern of an opaque circular obstacle (Tyler and Thompson, 1976) and we therefore gain insight about the detection efficiency and measurement accuracy of measuring cloud droplets with the holographic system. The size distribution of the CloudTarget disks is comparable to cloud droplets. The CloudTarget and the experimental procedure and analysis methods is in detail described in (Thiede et al., 2025b). The main principle is, that position and size of the disks printed onto the CloudTarget are well defined and the measured "particles" can then be compared to this ground truth. In the following the analysis is limited to the center $x$-$y$ region of the sample volume of 18.4 mm $\times$ 18.4 mm, which is about 50% of the camera sensor size. As detailed in Thiede et al. (2025b) recall, the rate of correctly detected and identified particles, is increased if the region close to the cross-sectional bounds (effectively the camera sensor cross-section) of the holographic sample volume are excluded from the analysis. The 18.4 mm were chosen as they exclude a minimum section of 2 mm from any edge and a square cross-section was found to be optimal.

#### 3.2.1 Droplet Detection Recall

From the one-to-one matching of measured particles and the known ground truth particles we can calculate the detection efficiency of HoloTrack (combined with losses in the processing steps) in terms of recall. Recall is defined as

$$\text{Recall} = \frac{TP}{TP+FN} = \frac{TP}{P}\ , \tag{5}$$

where $TP$ is the number of true positive particles, i.e. real particles correctly measured and identified as such, $FN$ is the number of false negatives, which are real particles not detected by our system. $TP$ and $FN$ therefore make up the number of total real particles, the "positives" $P$. Recall is therefore a measure of how many of the actual droplets were correctly found by the instrument.

We found that CloudTarget is not suitable for accurate measurement of precision (~~of the droplets that were found, how many~~ also known as positive predictive value, which indicates the fraction of detected droplets that are actually droplets and not False Positives) due to the occurrence of "ghost" particles through reflections on the glass surfaces (Thiede et al., 2025b) but accuracy in terms of false positive detections is further discussed in ~~section~~ Section 3.3.1.

In Figure 8 we present the measured recall for measurements with the CloudTarget at different $z$-distances from the image plane as a function of ground truth ~~size~~ diameter $d_{gt}$ of the printed circles. As mentioned above, the camera window is at reconstructed $z = 2.5$ cm and the laser window at $z = 22$ cm. The general trend, as expected for any in-line holographic

system, is that recall decreases with increasing depth position $z$ especially for smaller droplets. If a reliable detection of 10 $\mu$m and larger droplets is desired, the measurement volume should be restricted to the sub-volume up to $z \approx 8.5$ cm.

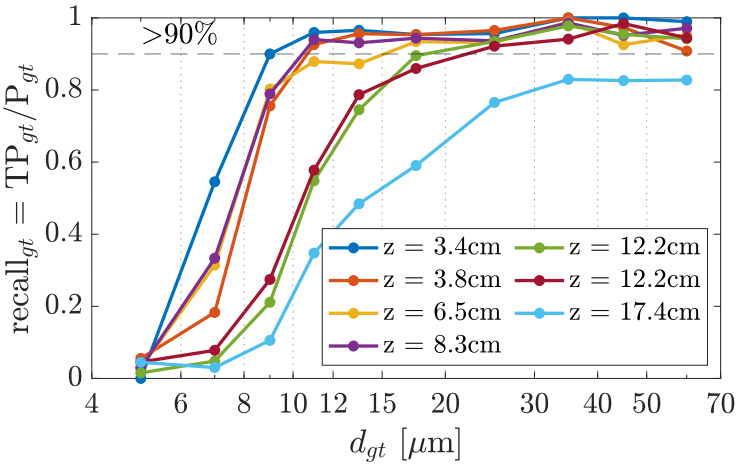


**Figure 8.** Recall measured with the CloudTarget as a function of ~~actual~~ the theoretical ground truth particle diameter ~~measured with the CloudTarget~~$d_{gt}$. The recall is determined within the center cross section of to 18.4 × 18.4 mm. A CloudTarget photomask was recorded with HoloTrack at different z-distances from the imaging plane. The holograms were automatically processed. Recall is a measure for detection efficiency and indicates how many of the actual particles were correctly found by the system. For $z \lesssim 8.5$ cm particles of 10 µm diameter or larger are reliably detected. The results are binned by ground truth diameter $d_{gt}$, the diameter of the printed disks on the photomask which might vary slightly from the measured diameter $d_m$.

### 3.2.2 Velocity Uncertainty Estimation

~~To ultimately~~ To estimate the uncertainty in particle velocity measured from ~~the displacement of the particle~~ particle displacement, we analyze the ~~position or~~ particle-distance uncertainty ~~with~~ using the CloudTarget. For this, we assume that the inter-particle distance between two particles in ~~one hologram is the same as the~~ a single hologram is equivalent to the distance of one particle measured ~~in two different~~ across two holograms of a hologram pair. Since we do not expect particle position error to vary significantly from hologram to hologram, this is a fair assumption. From the $TP$ found in the CloudTarget test, we calculate all measured inter-particle distances $s_m$ and ~~according~~ the corresponding ground truth inter-particle ~~distance $s_m$. We find that the relative error of~~ distances $s_{gt}$. The measured inter-particle distances $s_m$ are corrected for potential $x$-$z$- and $y$-$z$-tilts of the CloudTarget. The error in inter-particle distance ~~depends on the distance itself, smaller measured~~ should only depend on the position uncertainties of both particles in each pair, and thus the absolute error is independent of distance. As discussed in Section 2.2.2, the uncertainty of the effective inter-frame time is negligible. Therefore, the constant absolute error in distance measurements translates directly to a constant absolute error in velocity measurements. Figure 9 shows a histogram of the deviations between measured and ground-truth inter-particle ~~distances have a larger uncertainty. The expected~~

~~inter-particle distances or in the case of particle tracking particle displacement we expect to measure in HoloTrack is directly linked to the mean velocity $\bar{u}$: $s_m \approx \bar{u}\Delta t$. In Figure 9 we therefore show the relative inter-particle distance error as a function of mean velocity for our current timing of $\Delta t = 500$ $\mu$s. The rms - error in distance measurement is below 1.5% for~~ distances, $s_{gt} - s_m$, for different $z$-positions within the sample volume. Generally, the RMS error increases with $z$. At $z = 6.5$ cm and $z = 17.4$ cm we additionally observe a systematic negative bias (measured distances exceed the ground truth). This bias is present even before tilt-correction, so it cannot be attributed to tilt or errors in the correction. A diverging beam could explain the over-estimation of distances at large $z$, but the measurements at $z = 12.2$ do not support this. Thus, the source of the bias remains unresolved. Measurements are typically restricted to lower $z$ due to low recall at high $z$ (see Section 4), so the bias is likely usually negligible. With an RMS distance error below 33 µm across all $z$~~-distances for the design velocity of about 10~~-positions, we estimate the upper-bound velocity uncertainty to be about 0.07 m/s ~~. Since the error in laser timing is negligible compared to the distance error, the distance error can directly be assumed to be the error in droplet velocity measurement. We expect any droplet measurements to decrease in accuracy with increasing $z$-position, including the position measurement. Therefore, it could also be argued that the measurement at $z = 12.1$ cm, showing overall highest deviation from ground truth, is an outlier and the actual rms-error is closer to 1%. In any case, the error can be reduced by increasing the~~ for an inter-frame ~~time e.g. for a mean velocity $\bar{u} \approx 5$ $m/s$ it would be advisable to increase $\Delta t$ to 1000 $\mu$sto achieve errors smaller than 1.5%.~~ time of 500 µs. This error can be further reduced by increasing the inter-frame time, although this reduces the overlapping volume within hologram pairs and thereby limits the volume in which velocity can be measured. For distances in the $z$-direction, the CloudTarget does not provide an absolute ground truth; however, we know that all particles should lie on a 2D plane. We find the RMS deviation from a plane fitted through the measured points to be 56, 99, 260 and 250 µm for $z$ =3.8, 6.5, 12.2 and 17.4 cm, respectively. For an inter-frame time of 500 µs, this translates to a $v$ velocity component RMS error of less than 0.5 m/s. However, extra care is warranted with non-optimal angles of attack for the $v$ component, since this component is most susceptible to interference from the camera and laser arms.

### 3.3 Holography Performance Evaluation and Characterization: Wind Tunnel Tests

For validation of the particle tracking velocimetry and flow measurement capabilities we performed test measurements with HoloTrack in the Prandtl Wind-Tunnel at MPIDS, which is an open circuit wind tunnel with a test section of 150 cm wide 130 cm high (Bodenschatz et al., 2014). The HoloTrack instrument was placed approximately in the center of the tunnel 8.5 m downstream from an active turbulence grid, consisting of >100 individual paddles square that can be controlled to change their opening angles (same active grid as described in Bodenschatz et al., 2014) and therefore increase turbulence. The sample volume was positioned 19 cm above the ground and at least 55 cm from the tunnel walls(see Figure 10).

We performed experiments at two fan rotation rates, i.e. at two different mean velocities: 3.8 m/s and 10.0 m/s (current timing settings optimized for 10 m/s) with the turbulence grid open, meaning only acting as a passive grid. At the design velocity of 10.0 m/s we also increased the turbulence by operating the active grid and we tested the influence of a yaw angle on the validity of measurements in the holographic sample volume. In each of the experiments, droplets were introduced into the flow at the position of the grid with a hand held pressure sprayer and holograms were recorded with the timing as explained in ~~section~~

~~CloudTarget reveal error in inter-particle distance measurements. We show the rms of the relative inter-particle distance error. The data is binned by inter-particle distance translated to mean velocity for the set inter-frame time of 500s. The shaded shaded area left from the vertical line corresponds to mean velocities smaller than the design velocity of 10 m/s, where the error is expectedly high. Increasing the inter-frame time would shift all curves towards left, i.e. decreases the error for the given velocities. This would be recommended for accurate velocity measurements with a smaller mean velocity. Again, the analysis cross-section reduced to the center 18.4 × 18.4mm in~~

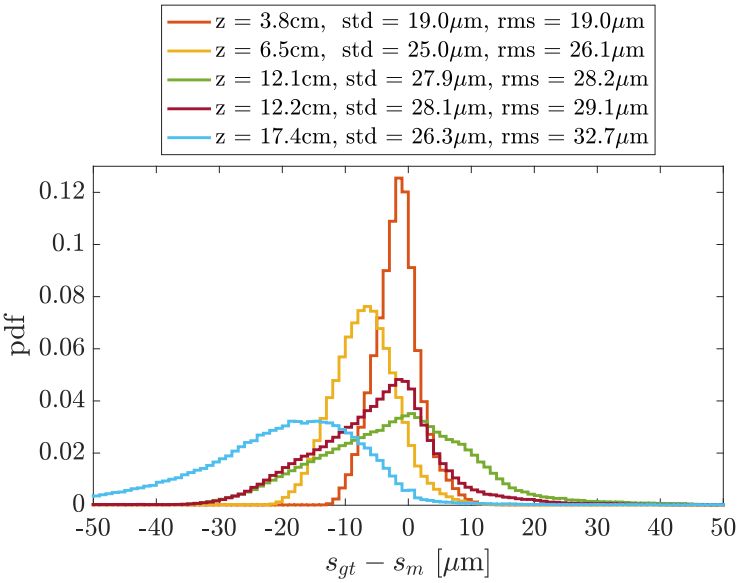


~~x-y.~~

**Figure 9.** CloudTarget reveals error in inter-particle distance measurements. Histograms of inter-particle distance error are shown as a function of sample volume depth $z$. The RMS distance error remains below 33 μm in all cases, corresponding to an upper-bound velocity error of 0.07 m/s for an inter-frame time of 500 μs. As before, the analysis cross-section is limited to the central 18.4 × 18.4 mm region in $x$-$y$.

Section 2.2.2 (hologram pairs at 25 Hz with inter-frame time of 500 μs). The recorded droplet sizes range from about 10 μm to 100 μm, but mostly >40 μm. From each hologram pair the droplet positions and size were extracted. The data recorded in the second frame "Holo ~~B~~$H_1$" are pre-shifted by the mean flow in $y$-direction (see Figure 10 for coordinate system) $u$ measured with the pitot tubes as a first guess. Afterward, for both Holo ~~A and Holo B~~$H_1$ and Holo $H_2$, binary 2D images of the projected particle positions in the $x$-$y$ plane are created.~~The particle sizes in these projections are artificially enlarged, weighted by the square root, to enhance overlap between matched particles. d~~ By identifying the maximum of the two-dimensional correlation coefficient between the two images, the actual mean displacements in the $x$ and $y$ directions, $\Delta\bar{s}_x$ and $\Delta\bar{s}_y$, are determined. The particle sizes in these projections are artificially enlarged, weighted by their square root, to enhance weight of small particles in the correlation. Within the overlapping region of the 18.4 mm × 18.4 mm center (blue and red square in Figure 10) regions of each holograms the particles are matched from Holo ~~A to Holo B~~$H_1$ to Holo $H_2$. For this, we search for matches within 500μm (~~dark blue~~ pink square in top left of Figure 10 A) in $x$-$y$, 2 mm in $z$ and an offset of 8μm or 20% of the diameter,

which ever is lower. If more than one potential match is found, the closer match in position and size is selected. This simple matching procedure worked well for the sparsely populated Wind Tunnel Test Holograms but might need to be replaced with more sophisticated algorithms (e.g. Baek and Lee, 1996) or stricter rules for in-situ cloud droplet holograms.

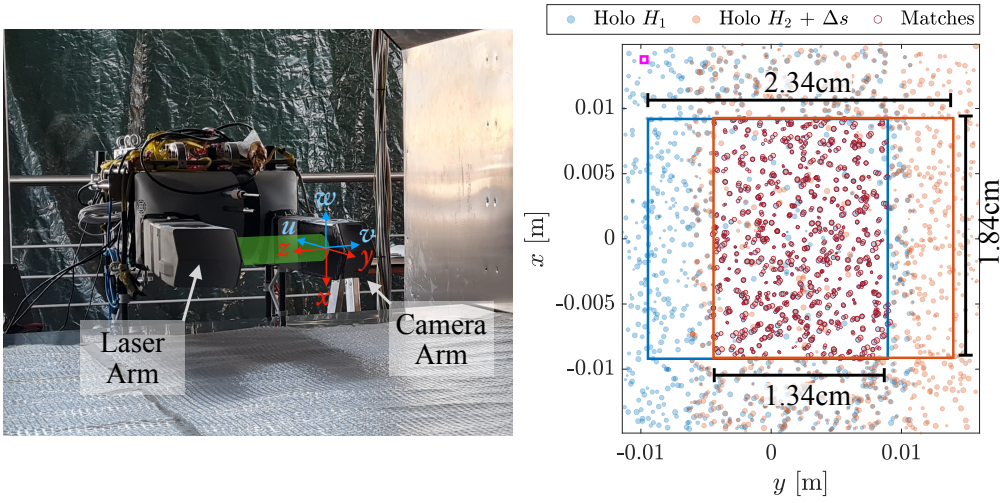


**Figure 10.** Left: HoloTrack placed in Wind Tunnel for evaluation of particle tracking. The y-axis of the sample volume is aligned with the mean flow direction $u$ in the non-yawed experiments. The sample volume is 19 cm above ground. Right: Examples of particles measured in a hologram pair, that consists of hologram ~~A~~ $H_1$ and ~~B~~$H_2$. For each hologram the center $x$-$y$ cross section of 18.4 × 18.4 mm is considered (shown as red and blue square) and matching is performed in the overlapping region. Particles that are considered a match are marked with a dark red outline and need to be within 500µm in $x$-$y$ after mean shift (indicated by small ~~dark blue~~ pink square) and within 2mm in $z$ to each other, and can only deviate 20% (or 8µm) in diameter to be considered a match.

### 3.3.1 Particle Match Rate and False Detection Rate

Before discussing the velocity measurements, we discuss the efficiency of droplet detection, which complements the Cloud-Target results presented above. Through the matching, developed to analyze particle velocities, we can extract further information about how much we can trust the extracted particle data. From all the particles measured (i.e Predicted Positives) in the overlapping region in Hologram ~~A~~ ($PP_A$ $H_1$ ($PP_{H1}$) a fraction can also be found in Hologram ~~B~~$H_1$, which we denote with ~~$PP_{A\wedge B}$~~ $PP_{H1\wedge H2}$. This ratio of particles that can be found in both holograms of a hologram pair to the total number of particles in one of the holograms we define as the Particle Match Rate $PMR$:

$$PMR_{AH1} = \frac{PP_{A\wedge B}}{PP_A} \frac{PP_{H1\wedge H2}}{PP_{H1}}. \tag{6}$$

We calculate the $PMR$ for 100 Hologram pairs of the wind tunnel test at two different velocities, so at two different shifts between holograms. Here, we use the ~~less turbulent data from the experiments with~~ data from experiments with lower turbulence

where we used an open i.e. passive grid as we expect our simple matching algorithm to be even more reliable in less turbulent flows. In Figure 11, we show the $PMR$ for different $z$-positions (positions of CloudTarget measurements $\pm$1cm each) as a function of measured particle diameter $d_m$. We see a clear trend that match rate is both particle size and $z$-position dependent. This trend was expected as $PMR$ is directly tied to recall.

Combining the results for Particle Match Rate with the recall measurements with the CloudTarget (see ~~section~~ Section 3.2.1)

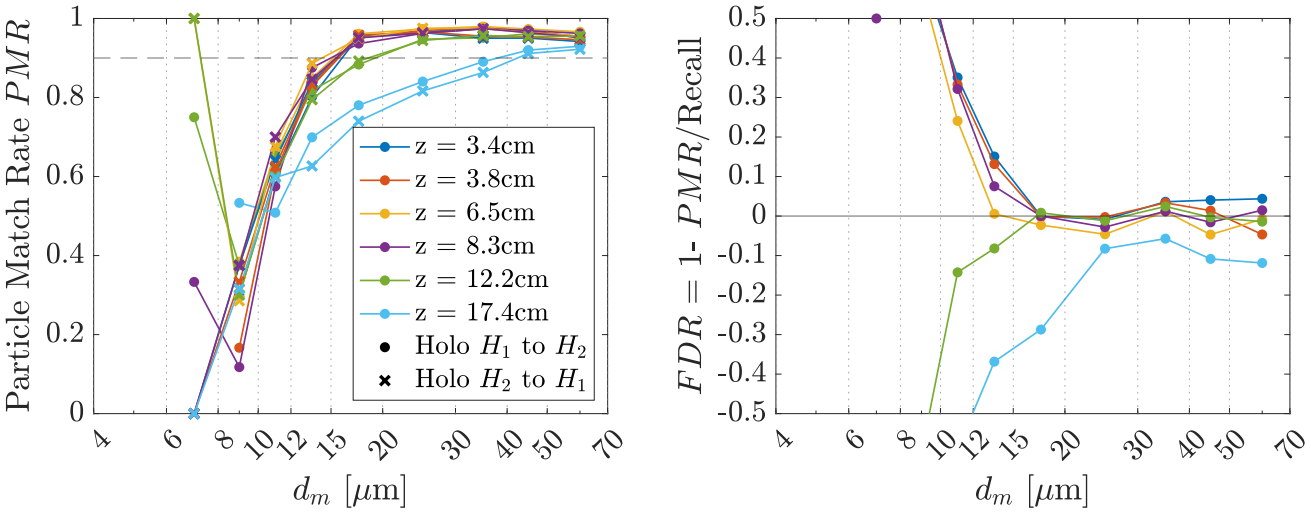


**Figure 11.** Left: Particle Match Rate as a function of measured diameter for the same $z$-positions used in the CloudTarget Test (each z corresponds to $z \pm 1$cm). The Match Rate is calculated based on the overlapping cross sectional regions of 18.4 $\times$ 18.4 mm and is a measure for how many of the measured particles are found in both hologram ~~A~~ $H_1$ and ~~B~~ $H_2$. Right: Taking the recall determined with CloudTarget into account allows an estimation of $FDR$, which independently of $z$-position is negligible for particles larger than 15$\mu$m. For smaller particles, the total number of sampled particles were too low in the Wind Tunnel tests to draw reliable conclusions.

allows us to determine the False Discovery Rate $FDR$ and therefore a measure of False Positives $FP$. The idea follows the simple argument, that only real particles are matched from hologram to hologram as noise that produces $FP$ would not be displaced with approximately the mean velocity which is a requirement for matching. If the recall is known a certain $PMR$ can be expected. If the $PMR$ is lower than this expected value, we assume False Positives to be the cause. We start with the definition of the Particle Match Rate and assume that there is no accidental matching, from which follows that all matched particles are True Positives ~~$PP_{A\wedge B} = TP_{A\wedge B}$~~. $PP_{H1\wedge H2} = TP_{H1\wedge H2}$.

$$PMR_{AH1} = \frac{PP_{A\wedge B}}{PP_A}\frac{PP_{H1\wedge H2}}{PP_{H1}} = \frac{TP_{A\wedge B}}{TP_A + FP_A}\frac{TP_{H1\wedge H2}}{TP_{H1} + FP_{H1}} = \frac{1}{\frac{TP_A}{TP_{A\wedge B}} + \frac{FP_A}{TP_{A\wedge B}}}\frac{1}{\frac{TP_{H1}}{TP_{H1\wedge H2}} + \frac{FP_{H1}}{TP_{H1\wedge H2}}} \tag{7}$$

We know that ~~Recall$_A = \frac{TP_A}{P}$~~ Recall$_{H1} = \frac{TP_{H1}}{P}$ and the probability, assuming the particle measurements in holograms ~~A and B~~ $H_1$ and $H_2$ are completely independent, for particles to be found in both holograms ~~A and B is $\frac{TP_{A\wedge B}}{P} =$ Recall$_A^2$~~ $H_1$ and

$H_2$ is $\frac{TP_{H1 \wedge H2}}{p} = \text{Recall}^2_{H1}$. With that it directly follows

$$FDR_{AH1} = \frac{FP_A}{PP_A}\frac{FP_{H1}}{PP_{H1}} = 1 - \frac{PMR_A}{\text{Recall}}\frac{PMR_{H1}}{\text{Recall}} \,. \tag{8}$$

The ~~FDR~~ $FDR$ (averaged over ~~the hologram pairs~~ $H_1$ and $H_2$ of each hologram pair) is shown in Figure 11 ~~B. The measurement~~ on the right. The calculated $FDR$ fluctuates around 0 for particles with $d_m$ >15µm for all $z$, which indicates that there are almost no $FP$ ~~are present in the holograms~~found. Negative values of $FDR$ as observed for small particles and large $z$ are not physical and therefore indicate ~~a measurement uncertainty that consists of the uncertainty~~ an uncertainty in this method of evaluating the $FDR$. This uncertainty is a combination of uncertainty in particle matching $PMR$ and the uncertainty in measuring the recall with the CloudTarget specifically for large $z$ and small $d_m$. Especially for $z = 17.4$ cm we argue that the recall measurement with CloudTarget probably ~~underestimates~~ underestimated the actual recall~~as there is no reason to believe the matching~~, which then leads to negative $FDR$, as it is unlikely that the matching used to calculate $PMR$ was especially bad at high z. For smaller particles $d_m < 12$ $\mu$m the measurements become unreliable. This is indicated by a negative $FDR$ for ~~$z = 12.1$~~$z = 12.2$ cm and 17.4 cm. Moreover, less than 1.5% of the measured droplets had a diameter smaller than $12\mu m$, which translates to an average of less than 10 small droplets per hologram, so very few small False Positives $FP$ (order of $10^0$) or unmatched $TP$ could lead to this overestimation of $FDR$ here for small droplets in $z$ <10 cm ($FDR = FP/PP$, low number of predicted positives $PP$ in size bin means few $FP$ could lead to high $FDR$).

### 3.3.2 Droplet Velocity Measurement Evaluation

From the one-to-one particle matching between holograms ~~A and B~~ $H_1$ and $H_2$ the velocity of the individual particles can be calculated via $u = -\frac{\Delta y}{\Delta t}$, $w = -\frac{\Delta x}{\Delta t}$ where $u$ is the oncoming flow velocity and $w$ the vertical velocity. Due to high inaccuracies of measuring the $z$-positions of the particles (~~$10^2 \mu m$~~$10^2$ µm) and the obstruction caused by the arms, the $v$ component of the flow can not be accurately measured with the holographic system (see also Figure 13).

In Figure 12, we show the measured average particle velocity in the direction of the mean wind $u$ from the holographic system normalized by the velocity measured by the 3D pitot tube. ~~In both cases, the~~ The mean measured particle velocities and mean velocity measured by the 3D pitot tube agree remarkably well within an offset of less than 3.5% ~~throughout~~for two different mean velocities. Moreover, the measured velocity is reasonably constant throughout the whole $z$-range between the holographic arms ($z = 2.5 - 22$ cm) with slightly higher measured velocities for small $z$ as can be seen in Figure 12. For the lower velocity, we see that the standard deviation of the measured particle velocities (indicated with error-bars) exceeds the standard deviation from the pitot tube measurement (shaded region). At $\bar{u} = 10$ m/s also the standard deviation agrees well. This is caused by the inter-frame time being 500 $\mu$s in both cases, hence leading to a smaller displacement $\Delta s_y$ in the lower velocity case~~, where the error of that displacement is estimated significantly larger with an rms of less than 3% compared to the rms at 10 m/s of less than 1.5% based on CloudTarget measurements~~. Since the absolute error in velocity is constant, the relative error becomes larger for lower mean velocity (see Figure 9). However, as explained earlier the error can be decreased by increasing the inter-frame ~~time can be adjusted by changing the timing of the holographic setup~~time depending on the mean velocity. To analyze HoloTrack's ability to measure fluctuating droplet velocities in a turbulent flow we compare results from experiments

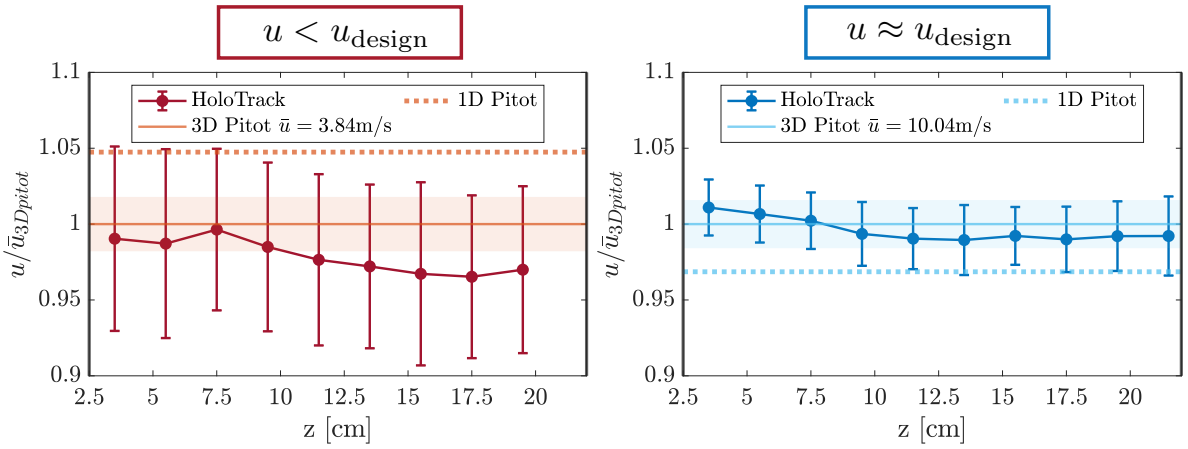


**Figure 12.** Particle velocity measured with HoloTrack as a function of position between the arms normalized with the mean velocity measured by the 1D pitot tube. ~~Errobars~~ Errorbars indicate the standard deviation of the measured droplet velocities from the holographic system and the shaded region indicated the standard deviation of velocities measured with the 3D pitot tube. The offset of the mean is smaller than 5% which shows the arms only have minimal effect on the flow if HoloTrack is directly oriented into the mean wind.

with an open grid to experiments with an active grid, increasing the turbulence in the flow. This analysis is restricted to the measurement volume that we propose as suitable in Section 4 to reliably detect droplets <10 µm (1.84 cm × 2.34 cm × 5 cm with 3.5 cm<$z$ <8.5 cm). In Figure 13 A and B we compare the probability density function (pdf) of the $u$-component of the 3D pitot tube with the pdf of the particle velocities measured with holography for a mean velocity of about 10 m/s with an open grid (~~lower turbulence intensity~~A: lower turbulence) and active grid (B: higher turbulence). For the open i.e. passive grid the mean velocities agree well as discussed but the 3D pitot tube measures ~~1.6% turbulence intensity, whereas we measure 2.2% with HoloTrack . However, the small velocity fluctuations here are close to the upper bound estimated error of 1.5% in velocity measurements of the holographic system.~~ velocity fluctuations of $u_{RMS} = \sqrt{\langle u' \rangle} = 0.16$ m/s, whereas HoloTrack measures higher $u_{RMS} = 0.19$ m/s. The estimated uncertainty of the pitot tube pressure sensor is 0.05 m/s at 10 m/s which is 0.5% and HoloTrack's uncertainty is 0.07 m/s the deviation is therefore within the estimated uncertainties. In the higher turbulence case with the active grid, ~~both~~ the 3D pitot tube and HoloTrack agree ~~on $TI = 3.7\%$~~well with $u_{RMS} = 0.38$ m/s (HoloTrack) and $u_{RMS} = 0.38$ m/s (pitot tube), which confirms the accurate measurement of the fluctuating velocities ~~if they exceed the estimated velocity error~~ further, especially when they are higher and the relative error decreases. The difference in measured mean velocity is only ~~1.3~~1.2%. This can not be exclusively explained by the pressure sensor uncertainty of the pitot tube (red shading). This slight offset could be caused by the two different measurement positions ~~and~~ of holographic system and pitot tube and effects of the geometry of the HoloTrack instrument box that only cause a difference in the measured mean velocity in case of higher turbulence.

We have to keep in mind however, that the pitot tubes can also not be considered a perfect ground truth and there might be

additional error sources besides the accuracy of the pressure sensors that can also shift the pitot tube results both for mean velocity as well as fluctuations.

In panels C and D of Figure 13, we show histograms of the velocity fluctuations in all three components. The grid configuration is expected to produce isotropic turbulence in the wind tunnel, so ideally all three components should agree. For the passive grid (Figure 13C), the fluctuations $u'$ and $v'$ agree remarkably well and $u_{\mathrm{RMS}} \approx w_{\mathrm{RMS}}$; for the active grid (Figure 13D), the agreement remains reasonable. The measured $v'$—the velocity fluctuations in the $z$-direction—however, exceed those of $u'$ and $w'$. This behavior is expected, since measurements uncertainties associated with the $v$-component of the flow velocity is larger as discussed above. In contrast, the Pitot tube reports significantly lower fluctuations in the $w$ component, with $w_{RMS} = 0.24$ m/s for the active and $w_{RMS} = 0.11$ m/s for the passive grid. Since Pitot accuracy decreases at low absolute velocities, also evident in a systematic offset for the mean velocity $\bar{w}$, its $w$-fluctuation values are less reliable. The comparison of $u$ and $w$ from HoloTrack is therefore likely more valid and supports the measured $w$ component. The holographic system should have no systematic differences between $x$- or $y$- direction. Minor deviations could be caused by the instrument geometry affecting $x$- and $y$-velocity components differently. The observed negative mean vertical velocity, stronger in the less turbulent case, hints toward sedimentation of the droplets in the wind tunnel experiments. This is further attested by the diameter dependent increasing negative $w$. Due to the limited data and to keep the scope of the paper clear, we refrain from further analyzing the relation in more detail here. Nonetheless, it showcases HoloTrack's useful feature of measuring droplet dynamics and size at the same time to investigate the dependence. Overall, we have seen that the velocity measurements of HoloTrack work as expected even with a very simple particle tracking algorithm. ~~Turbulence that exceeds the random error in inter-particle distances~~ Mean velocity and velocity fluctuations that exceed the uncertainty in velocity measurement of 0.07 m/s, can be accurately measured in $u$ (longitudinal) and $w$ (vertical) direction.

### 3.3.3 Influence of Instrument Yaw on Measurement Accuracy

To analyze the effects of the arms on the holographic sample volume specifically in the case of non-zero yaw angle of attack we recorded holograms with HoloTrack being yawed with respect to the mean flow in the wind tunnel. These tests were performed with the grid open to have a close to laminar flow and see clear blockage effect of the arms on the flow. We investigate 4 different yaw angles: $\alpha = 0°, 1°, 4°$ and $6°$. Here we define a positive yaw angle $\alpha$, when the flow has a negative $v$-component in $z$-direction as indicated in the schematic in Figure 14. We investigate positive yaw angles, as they are likely to have a stronger influence at the low $z$ region of the sample volume which is more critical due to the higher recall for small droplets at low $z$. As a first indication of influence of the holographic arms, specifically the tips, we show a "super-hologram" i.e. a heatmap of relative concentration of detected droplets. In cases of optimal and constant detection and randomly distributed droplets we expect this heatmap to be flat. Any deviations indicate varying detection or a non-random particle distribution. In Figure 14 the super-hologram is shown as projection in $x$-$z$ and $y$-$z$ (where $x$ was limited to the height of the arm tip, where the largest obstruction is) for the different yaw angles $\alpha$. In the case of no yaw we see that the region of <1 cm above the camera window shows lower particle concentration. This is caused by the boundary layer on the camera arm. For larger yaw angles we see that

the height of the void region increases and the particles expelled from the ~~arms wake~~ wake of the arm accumulate in a distinct layer of high relative concentration. The angle of this accumulation layer in the $x$-$z$-plane can be associated with the angled tip of the camera arm, where the tip aligns with large $x$ (bottom) of the camera. In the most extreme case of $\alpha \approx 6°$, the void and accumulation regions ~~are~~ reach up to $z \approx 6$ cm. The other less significant non-uniformaties in the concentration further away from the camera observed in all yaw angles can be associated to the $z$-position and diameter dependent recall and non-random particle positions due to the hand-held spray bottle producing the droplets (each super-hologram is from data recorded within few seconds and spraying more towards low or high $z$ can introduce a constant bias).

Another test, that is uniquely possible with HoloTrack is to analyze the influence of yaw angle of attack on the particle velocities. If the mean flow has a yaw angle of attack $\alpha$ in the $y$-$z$-plane with respect to the $y$-axis of the instrument, in an optimal undisturbed case we expect the same angle $\alpha_m = \alpha$ between the measured $u$ and $v$ component of the droplet velocities:

$$\alpha_m = \arctan\left(\frac{-v}{u}\right) . \tag{9}$$

In the previous section, we explicitly stated that the uncertainties in measuring droplet $z$-positions ~~are too high to reliably measure~~ and therefore in measuring the $v$-velocity component of individual droplets is high. By averaging over droplets over several holograms and the whole $x$-$y$-domain, we are however able to see a clear signal and analyze the average droplet angle as a function of $z$-position, which is shown for the four different yaw angles in Figure 14. The observed $\alpha_m \approx 0°$ for $\alpha = 0°$ demonstrate the validity of this approach and that the high $z$-position- and therefore $v$-component uncertainty is averaged out by our approach and we do not have any persistent bias.

For all yaw angles >$0°$, the observed velocity angle $\alpha_m$ in the center between the arms ($z = 12.25$ cm) is approximately the yaw angle of attack $\alpha$ and approaches $0°$ towards the arms. This means the flow aligns more with the direction of the holography arms the closer the $z$-position is to one of the arms.

We argue that quantities like concentration and size are largely unaffected by a slight deviation in velocity angle (change of $10°$ leads to change of <1 mm in position) but to accurately measure the droplet velocities and analyse clustering with e.g. the radial distribution function $RDF$ of the droplets, where the accurate and undisturbed positions of droplets are of utmost importance, the analysis should be restricted to holograms with low yaw angle and $z$-regions of the sample volumes, where the measured angle droplet angle is undisturbed $\alpha_m = \alpha$. Our observation in turbulent wind tunnel flow, not shown here, indicate that the arm influence is less significant but we suggest the same restrictions as we found in the laminar case should be used to be on the safe side.

## 4 Discussion

~~In prior sections, we elaborated on the construction, intentions, and performance assessment of the HoloTrack, an instrument designed for in-situ measurements of cloud droplets and laboratory experiments. Here, we evaluate the outcomes of these assessments and reflect on its current capabilities and potential improvements.The mechanical build of HoloTrack is robust~~

| | $d_m > 10\ \mu$m | $d_m > 15\ \mu$m |
|---|---|---|
| Particle Position and Size | 1.84 cm × 2.34 cm × 5 cm = **21.5 cm**$^3$ | 1.84 cm × 2.34 cm × 8.5 cm = **36.6 cm**$^3$ |
| Particle Velocity | 1.84 cm × 1.34 cm × 5 cm = **12.3 cm**$^3$ | 1.84 cm × 1.34 cm × 8.5 cm = **21.0 cm**$^3$ |

**Table 2.** Holographic sample volumes per hologram pair if the mean velocity leads to a displacement of 5 mm (e.g. current inter-frame time of 500 µs with a mean wind speed of 10m/s) at an angle of attack of 0°. To capture particle positions and their size the combined volume of both holograms can be used, for velocity measurement only the overlapping region is considered. We show volumes for two different minimal droplet diameters, where recall >90%. Multiplying values of the sample volume by 25 Hz, i.e. the HoloTrack double-frame acquisition frequency, provides the sampling volume per seconds.

~~and stable. It is designed to fit into both in-flight and laboratory environments. Future designs may, however, benefit from weight reduction.The electronic design is defined by its success in enabling a fully automated data logging and holography control program. One problem encountered when operating the sensors connected to the main HoloTrack computer was intermittent disconnections on instruments with a USB interface, which lasted a few seconds at most and affected some of the non-holographic measurements. Consequently, noncontinuous pitot-tube measurements were recorded in the test flight as explained in section 3.1, an issue that seems to be tied to ground loops existing in the current setup. Despite these disconnection issues, hologram recording remained unaffected, with no frames lost and consistent full frame rate recording.Extensive ground tests and the successful altitude triggering during the test flight show the success of the measurement automation. A further extension of trigger options such as detected droplets by the OPC-N3 or the CDP-2 would make HoloTrack even more efficient in ensuring holograms are only measured while in cloud. The integrated screen, which displays the measurement status and provides direct control of the holographic system, has proven highly beneficial in the laboratory, significantly reducing setup time and troubleshooting. It also renders the device entirely self-contained.From analysis of the recorded velocities from both pitot tubes during the test flight (as presented in section 3.1.3) we conclude that the 3D pitot tube provides the necessary accuracy to compute the dissipation rate, using the second-order structure function as the calculation method. Conversely, the 1D pitot tube was not usable in turbulence statistical analysis due to the filtering but served as a supplementary reference for mean velocity and can likely measure accurate turbulence data in future once the filtering is turned off. During wind tunnel experiments, pitot tubes started to malfunction after a certain period due to having excessive number of large drops produced by the hand sprays. Nevertheless, these tubes reliably recorded data throughout the test flight in non-precipitating clouds. Hence, we think that they might only be compromised after prolonged exposure in heavily precipitating clouds, where the presence of larger droplets mirrors the conditions of our wind tunnel experiments.Overall, the holographic system of HoloTrack works as expected. Here, the analysis is limited to the optimal 18.4 × 18.4 mm center in $x$-$y$. Droplets up to a minimal diameter of~~

### 4.1 Reliable Holography Sample Volumes for Droplet Position and Velocity Analysis

Table 2 quantifies the sampling volumes for two droplet sizes ($d_m$ >10 ~~mean then reliably detected up to $z = 8.5$cm. For hologram processing the pipeline optimized for the holographic system of the MPCK$^+$was used here. While the Neural Network was exclusively trained on MPCK$^+$data, detection accuracy and efficiency (quantified by $FDR$ and recall) are remarkably high. Further improvements, e.g. the detection of smaller particles, might be achieved by fine-tuning thresholds and the classification neural network specifically to HoloTrack.The implemented timing with~~ µm and $d_m$ >15 µm) at a mean wind of 10 m/s, where the current inter-frame time of 500 µs ~~was chosen to be optimal for a mean velocity of 10 m/s. In this velocity range, we found the maximal expected droplet velocity error to be smaller than 1.5% (<1% if we exclude clear outliers). We see that the velocities and velocity fluctuations measured with HoloTrack overall agree well with the 3D pitot tube measurements. If smaller mean velocities are expected, the timing should be changed so that the mean displacement is still on the order~~ corresponds to a displacement of 5 mm~~≈ 1600 px. In instances demanding higher accuracy in velocity, particularly in the precise detection of minor velocity fluctuations in low-turbulence flows (see section 3.3), adjusting the timing can increase the mean displacement and hence reduce the velocity error. This, however, would reduce the overlapping cross-section further~~. For particle positions and sizes, the combined volume of both holograms can be used, while for velocity only the overlap volume applies. For example, at ~~a~~ 10 m/s~~wind~~, doubling the inter-frame timing from 500 µs to 1000 µs, ~~so~~ thus increasing the mean displacement from 5 mm to 10 mm, decreases the overlap volume by 38%. ~~Table 2 provides a quantitative characterization of HoloTrack's sampling volumes for two droplet sizes (10 and 15 m), based on the current mean displacement at 10m~~The velocity RMS error is however reduced from 0.07 m/s ~~of 5 mm . Holographic sample volumes per hologram pair if the mean velocity leads to a displacement of 5 mm (e.g. current inter-frame time of 500 s with a mean wind speed of 10m/s) at an angle of attack of 0°. To capture particle positions and their size the combined volume of both holograms can be used, for velocity measurement only the overlapping region is considered. We show volumes for two different minimal droplet diameters, where recall >90%. Multiplying values of the sample volume by 25 Hz, i.e. the HoloTrack double-frame acquisition frequency, provides the sampling volume per seconds. For in-situ cloud droplet data recorded with HoloTrack, we plan to optimize the sizing algorithm to each dataset with the inverse threshold-independent method discussed in (Lu et al., 2012). Another measure for sizing uncertainty can then also be the two independent measurements for each particle measured in both holograms of a pair. As discussed in (Thiede et al., 2025b) sizing can not be evaluated with the CloudTarget if a threshold-based sizing method is used.In the wind tunnel evaluation experiments, we used a simple particle matching algorithm which was able to accurately match individual particles. This is a crucial advance over traditional two-dimensional Particle Image Velocimetry (PIV), which typically identifies shifts in composite patterns of multiple particles. Assisted by the availability of data on particle size and depth (z-position), the algorithm allows for targeted matching of individual particles. For higher droplet concentrations and~~to 0.03 m/~~or higher turbulence levels than present in the wind tunnel experiments presented here, which would be expected in in-situ cloud droplet holograms, more advanced matching algorithms would however likely be needed (e.g. Baek and Lee, 1996). By combining the matching results from droplets recorded in the wind tunnel experiments with the recall measurements from CloudTarget, we found that false detection rate i.e. false positive particles are negligible in the holographic droplet data processed as described in (Thiede et al., 2025b). This verification procedure can be replicated with in-situ droplet data, ensuring if in potentially more noisy in-situ holograms false positives are still negligible.In the test flight,~~

~~the observed yaw angle of attack of the mean flow, relative to HoloTrack's y-axis, demonstrated only moderate variations~~ s. This highlights the trade-off between velocity uncertainty and overlapped volume.

Droplets with a minimal size of 10 µm can be reliably detected up to $z = 8.5$ cm, and those larger than 15 µm up to $z = 12$ cm, when restricted to the optimal $18.4 \times 18.4$ mm center in $x$–$y$. To avoid influence of the camera arm the sample volume should additionally be restriced to $z > 3.5$ cm at 0° yaw angle. The resulting reliable volumes are shown in Table 2.

Yaw angle during test flights was modest, with a standard deviation of ~~6°. This was the case even though HoloTrack was freely suspended from the MPCK lower Helikite, confirming the instrument's design successfully aims to align~~ 6°, confirming that the suspension design aligns the instrument with the mean flow. ~~By varying HoloTrack's yaw relative to the mean flow during wind tunnel tests, we examined how obstructing tips and arms affect droplet concentration and velocity direction. Even at the~~ Wind tunnel experiments showed that even at optimal 0° yaw, ~~measurements are only valid for $z > 3.5$ cm (1 cm away from the camera arm). Analogous considerations apply to the laser arm , though the arms are not symmetric.~~ valid measurements are restricted to $z > 3.5$ cm to avoid arm obstruction. Based on these constraints, the resulting reliable volumes are shown in Table 2.

For yaw angles ~~$\alpha > 1°$, the arm influences droplet concentration~~ $|\alpha| > 1°$, concentration and velocity are affected up to $z = 6$ ~~cm and velocity direction at even larger $z$. Resolving $10\,\mu$m particles further restricts $z < 8.5$ cm. Hence, for accurate velocity measurements (including fluctuations) and~~ cm or more. Therefore, for airborne high-precision velocity or position-sensitive analyses (e.g., ~~radial distribution function), we exclude holograms with $|\alpha| > 1°$ for airborne measurements. For less position-sensitive measurements (e.g., size distribution, concentration), holograms at higher yaw are still usable with a suitably restricted sub-volume. If $z < 8.5$ cm is required for $10\,\mu$m particles and high-precision data, about 15% of the test flight holograms remain valid when $-1° < \alpha < 1°$. Restricting $z > 5.5$~~ turbulence fluctuations, RDF), only holograms with $|\alpha| < 1°$ provide sufficient data. But even in these the reliable volume is significantly reduced. For $|\alpha| < 1°$, $z > 5.5$ cm ensures $\alpha_m \approx \alpha$ and constant concentration, ~~giving a sub-volume of $1.84\,\text{cm} \times 1.34\,\text{cm} \times 3\,\text{cm} \approx 7.4\,\text{cm}^3$ per hologram, which corresponds to about~~ yielding $1.84 \times 1.34 \times 3$ cm $\approx 7.4$ cm$^3$ per hologram. As an example, if the holograms in HoloTrack's maiden flight were not overexposed and could have been analyzed, this would have amount to ~34 ~~Liters sampled over a 6750 m transect (~~ L of high-accuracy holographic data over a 20 ~~min)~~ min, 6.7 km transect (assuming only 15% of ~~the time $|\alpha| < 1°$. In~~ holograms are valid due to yaw angle). For comparison, a ~~CDP-2 probe would sample ~ 1.6 L, while~~ typical cloud droplet probe (e.g. CDP-2, Droplet Measurement Technologies) probe samples ~1.6 L and the state-of-the-art ~~holographic instrument of the MPCK$^+$ would sample ~ 180 L (assuming a perfect angle of attack 100% of the time). HoloTrack~~ MPCK$^+$ holographic system ~180 L under ideal conditions. HoloTrack is unique, however, ~~is the only imaging instrument measuring droplet velocity and providing two independent measurements of~~ in providing simultaneous droplet imaging and velocity measurements, with two independent size/position estimates per particle.

### 4.2 Limitations and Potential Future Improvements

Future designs of HoloTrack could benefit from weight reduction and ideally the occasional USB disconnections that affect non-holographic sensors can be fixed. Increasing the disk space of the ~~same sample volume, thereby increasing the accuracy of~~

cloud microphysical parameters. Note that these numbers are based on one scenario; the actual in-flight yaw might be stronger or weaker, changing the total usable volume for high-precision analyses. This can be easily verified from the measurements directly. The total number of holograms that can be recorded in flight could be increased by upgrading the hard disks holographic system (currently RAID0 of 4x1 TB disks) , the writing speed of the disks needs to be >3.25 GB/s to ensure operation at 50 Hz. There are currently 8 TB SSDs that fulfil these specifications, which would increase the runtime from 20 minutes to 160 minutes. Moreover, in any non-flight settings, the arms of HoloTrack can be positioned such that obstruction and therefore influence is minimal. To increase the fraction of total sampled volume that can be analyzed even for high accuracy analysis like velocity fluctuations and RDF there are several options. Solutions with the current design of HoloTrack would be to hang it such that the with 4× 1TB disks) can extend recording duration and total sample volume per flight. If new hard disks have even higher writing speeds, holograms could also be recorded in 10bit resolution, potentially enhancing detection. This potential effect of higher 10bit resolution on droplet detection can be evaluated with CloudTarget.

In wind tunnel tests, pitot tubes malfunctioned under heavy spray of large droplets but performed reliably in non-precipitating test flights, suggesting they only fail under extended exposure to precipitation-like conditions. HoloTrack's holograms were processed with the method of (Thiede et al., 2025b), achieving recall above 90% and negligible false positives for droplets down to 10 µin a defined sub-volume. The classification neural network is only trained on MPCK$^+$flight data and even better results may be achieved by fine-tuning the network with HoloTrack training data. The $FDR$ can be estimated again for flight-data to ensure in-situ-specific noise does not increase it significantly.

For in-situ applications, we plan to optimize sizing with the inverse threshold-independent method (Lu et al., 2012). HoloTrack's dual holograms per pair also allow an independent sizing uncertainty estimate. For higher turbulence and droplet concentrations than in our wind tunnel tests, more advanced particle matching algorithms (e.g. Baek and Lee, 1996) will likely be necessary.

Potential design refinements to mitigate the strong effect of yaw angle on the reliable hologram sub-volumes include: hanging HoloTrack with vertical $z$-axis is vertical, which would mean no obstruction by the arms if vertical velocity of HoloTrack is negligible (i.e. for constant altitude flights), similar to the MPCK$^+$design. This has the disadvantage that droplets could persist on the lower arm window although this would mostly be a problem in precipitating clouds. Another option would be to stabilize HoloTrack in yaw direction $y-z$-plane by hanging it from more than one single point.Furthermore, the (removing arm obstruction but risking window wetting in precipitation), stabilizing yaw with multi-point suspension, or optimizing 3D-printed arm cover could be exchanged, specifically several tip designs could be designed and evaluated in the wind tunnel as we did here, to find a more optimal design.arm tips. A key lesson is that superholograms, though widely used to evaluate holographic measurement biases, "superhologram" reconstructions alone cannot reveal all aerodynamic disturbances. While their effects on positional accuracy can often be mitigated in RDF calculations with minimal impact, they can more strongly affect turbulence measurements. This is especially relevant on low-airspeed platforms like drones or aerostats, where the angle of attack is harder to control. Only careful velocity calibrations , such as those presented here , can fully expose , especially in turbulence; only velocity calibrations as presented here can identify and correct these effects. With HoloTrack, we can correct or filter out the affected regions or holograms directly from the measurements to address these disturbances.

## 5 Conclusions

Overall, the evaluation ~~has shown~~ confirms that HoloTrack is a ~~very powerful and capable instrument both for~~ powerful instrument for both laboratory and in-flight ~~measurements. To summarize~~ studies of cloud droplet microphysics. In the following we summarize the key points and results of evaluation tests:

- HoloTrack is a fully autonomous ~~and automated measurement system that includes a powerful,~~ system that integrates a high-accuracy holographic ~~system and sensors to quantify the environmental conditions such as flow characteristics, instrument motion, temperature, pressure and relative humidity. It was successfully designed to work autonomously in flight operation on the MPCK platform and for easy operator control~~ sensor with environmental monitoring. It operates both in-flight and in laboratory settings with minimal operator input.

- The holographic system ~~reliably~~ records 25 hologram pairs per second, ~~where the~~ with adjustable inter-frame time~~within pairs can be freely adjusted to the desired displacement of particles. From each hologram pair we get two independent measurements of particle position, size and shape and one measurement of the particle velocity for all particles in the overlapping volumes.~~ . At 500 µs, the in-plane velocity RMS error is less than 0.07 m/s while for the transversal component it ranges between 0.1-0.5 m/s depending on the $z$-position, but timing can be adapted to match expected wind speed and accuracy needs.

- ~~To analyze HoloTrack the processing optimized for the MPCK$^+$in (Thiede et al., 2025b) achieves >90% recall and high precision for~~ For particles down to ~~10 $\mu$m~~10 µm, recall exceeds 90% up to $z = 8.5$ cm~~which results in a~~ , providing a reliable sample volume of 21.5 cm$^3$ (3D positions) or 12.3 cm$^3$ ~~for~~ (3D velocities) per hologram pair. ~~The reliable volume needs to be further reduced depending on desired velocity and particle position accuracy due to the obstruction of the holographic arms, especially in the case of non-zero yaw. In the test flight HoloTrack would still have sampled 34000 cm$^3$ of high-accuracy holographic data including droplet velocities over a horizontal transect of 6.7 km~~As an example, based on yaw measurements and defining reliable unobstructed sub-volumes, we estimate ∼34 L of high-precision holographic data would have been usable of the holograms in HoloTrack's maiden flight (if the holograms were not overexposed due to a broken pinhole).

- ~~We are able to successfully measure droplet velocities and fluctuations by tracking measured droplets within hologram pairs. We saw good agreement of measured longitudinal droplet velocity~~ Longitudinal droplet velocity ($u$~~with pitot tube measurements and expect the same accuracy for measurement of vertical velocities~~ ) agrees well with Pitot tube data, and isotropy of $u$ and $w$ ~~. The current inter-frame time of 500 s introduces a maximal error of 1.5% in velocity measurements where the mean velocity is around 8-10m/s. Due to the flexible timing options in HoloTrack the inter-frame time can be adjusted to desired accuracy for the expected mean velocity , making it a versatile instrument~~fluctuations in grid turbulence further confirms the reliability of the velocity measurements, including small velocity fluctuations for in-plane components of $u$ and $w$.

– By resolving ~~individual particle sizes and velocities, the effect of locally measured turbulenceon larger droplets can be analyzed as a function of Stokes number, potentially revealing mechanisms explaining a higher collision rate~~both size and velocity of individual particles, HoloTrack enables studies of turbulence–induced particle interaction of spherical and non-spherical particles.

*Code and data availability.* Evaluation datasets and code are available from the authors upon reasonable request.

*Author contributions.* BT and GB designed and developed HoloTrack with help of EB. FN contributed the code for saving holograms to disks in real time BT, YK and GB performed WindTunnel experiments. BT analyzed the holographic data from the performance evaluation experiments and YK calculated the dissipation rate from in-flight pitot tube measurement. All authors interpreted the results. BT wrote initial draft of the manuscript. All authors contributed to the final version of the manuscript.

*Competing interests.* The authors declare no competing interests.

*Acknowledgements.* We thank the MPIDS machine shop, led by Andre Heil, for designing and manufacturing HoloTrack's mechanical setup. We also extend our gratitude to the MPIDS research electronics team, particularly Laura Diaz-Maue, for designing the electronic components of the communication and power systems, and Holger Nobach, for advising on laser safety and for the development of the sequence generator. We thank Venecia Chavez-Medina and Hossein Khodamoradi for providing codes and advice for the use of the environmental sensors. Many thanks to the entire IMPACT campaign team for enabling the success of the campaign and the test flight.

This work was partly supported by the Fraunhofer–Max Planck cooperation program through the TWISTER project. Birte Thiede was financially supported by a fellowship of the IMPRS for Physics of Biological and Complex Systems.

## References


Allwayin, N., Larsen, M. L., Glienke, S., and Shaw, R. A.: Locally narrow droplet size distributions are ubiquitous in stratocumulus clouds, Science, 384, 528–532, 2024.

Baek, S. and Lee, S.: A new two-frame particle tracking algorithm using match probability, Experiments in Fluids, 22, 23–32, 1996.

Beals, M. A., Fugal, J. P., Shaw, R. A., Lu, J., Spuler, S. M., and Stith, J. L.: Holographic measurements of inhomogeneous cloud mixing at the centimeter scale, Science, 350, 87–90, 2015.

Beals, M. J.: Investigations of Cloud Microphysical Response to Mixing Using Digital Holography, Ph.D. thesis, Michigan Technological University, ISBN 9781303736155, http://digitalcommons.mtu.edu/etds/669, 2013.

Bertens, G., Bagheri, G., Xu, H., Bodenschatz, E., and Moláček, J.: In situ cloud particle tracking experiment, Review of Scientific Instruments, 92, 2021.

Bodenschatz, E., Malinowski, S. P., Shaw, R. A., and Stratmann, F.: Can we understand clouds without turbulence?, Science, 327, 970–971, 2010.

Bodenschatz, E., Bewley, G. P., Nobach, H., Sinhuber, M., and Xu, H.: Variable density turbulence tunnel facility, Review of Scientific Instruments, 85, 2014.

Borrmann, S., Jaenicke, R., and Neumann, P.: On spatial distributions and inter-droplet distances measured in stratus clouds with in-line holography, Atmospheric research, 29, 229–245, 1993.

Brown, P. R.: Use of holography for airborne cloud physics measurements, Journal of Atmospheric and Oceanic Technology, 6, 293–306, 1989.

Chávez-Medina, V., Khodamoradi, H., Schlenczek, O., Nordsiek, F., Brunner, C. E., Bodenschatz, E., and Bagheri, G.: Max Planck WinDarts: High-Resolution Atmospheric Boundary Layer Measurements with the Max Planck CloudKite platform and Ground Weather Station–A Data Overview, Earth System Science Data Discussions, 2025, 1–22, 2025.

Desai, N., Liu, Y., Glienke, S., Shaw, R. A., Lu, C., Wang, J., and Gao, S.: Vertical variation of turbulent entrainment mixing processes in marine stratocumulus clouds using high-resolution digital holography, Journal of Geophysical Research: Atmospheres, 126, e2020JD033 527, 2021.

Forster, P., Storelvmo, T., Armour, K., Collins, W., Dufresne, J.-L., Frame, D., Lunt, D., Mauritsen, T., Palmer, M., Watanabe, M., Wild, M., and Zhang, H.: The Earth's Energy Budget, Climate Feedbacks, and Climate Sensitivity, in: Climate Change 2021: The Physical Science Basis. Contribution of Working Group I to the Sixth Assessment Report of the Intergovernmental Panel on Climate Change, edited by Masson-Delmotte, V., Zhai, P., Pirani, A., Connors, S., Péan, C., Berger, S., Caud, N., Chen, Y., Goldfarb, L., Gomis, M., Huang, M., Leitzell, K., Lonnoy, E., Matthews, J., Maycock, T., Waterfield, T., Yelekçi, O., Yu, R., and Zhou, B., pp. 923–1054, Cambridge University Press, Cambridge, United Kingdom and New York, NY, USA, https://doi.org/10.1017/9781009157896.009, 2021.

Fugal, J. and Shaw, R.: Cloud particle size distributions measured with an airborne digital in-line holographic instrument, Atmospheric Measurement Techniques, 2, 259–271, 2009.

Fugal, J. P., Schulz, T. J., and Shaw, R. A.: Practical methods for automated reconstruction and characterization of particles in digital in-line holograms, Measurement Science and Technology, 20, 075 501, 2009.

Glienke, S., Kostinski, A. B., Shaw, R. A., Larsen, M. L., Fugal, J. P., Schlenczek, O., and Borrmann, S.: Holographic observations of centimeter-scale nonuniformities within marine stratocumulus clouds, Journal of the Atmospheric Sciences, 77, 499–512, 2020.

Grabowski, W. W. and Wang, L.-P.: Growth of cloud droplets in a turbulent environment, Annual review of fluid mechanics, 45, 293–324, 2013.

Grosvenor, D. P., Sourdeval, O., Zuidema, P., Ackerman, A., Alexandrov, M. D., Bennartz, R., Boers, R., Cairns, B., Chiu, J. C., Christensen, M., et al.: Remote sensing of droplet number concentration in warm clouds: A review of the current state of knowledge and perspectives, Reviews of Geophysics, 56, 409–453, 2018.

Henneberger, J., Fugal, J. P., Stetzer, O., and Lohmann, U.: HOLIMO II: a digital holographic instrument for ground-based in situ observations of microphysical properties of mixed-phase clouds, Atmospheric Measurement Techniques, 6, 2975–2987, 2013.

Hinsch, K. D.: Holographic particle image velocimetry, Measurement Science and Technology, 13, R61, 2002.

Hinsch, K. D. and Herrmann, S. F.: Holographic particle image velocimetry, 2004.

Jameson, A. and Kostinski, A.: What is a raindrop size distribution?, Bulletin of the American Meteorological Society, 82, 1169–1178, 2001.

Korolev, A., Emery, E., and Creelman, K.: Modification and tests of particle probe tips to mitigate effects of ice shattering, Journal of Atmospheric and Oceanic Technology, 30, 690–708, 2013.

Korolev, A., McFarquhar, G., Field, P. R., Franklin, C., Lawson, P., Wang, Z., Williams, E., Abel, S. J., Axisa, D., Borrmann, S., et al.: Mixed-phase clouds: Progress and challenges, Meteorological Monographs, 58, 5–1, 2017.

Larsen, M. L., Shaw, R. A., Kostinski, A. B., and Glienke, S.: Fine-scale droplet clustering in atmospheric clouds: 3D radial distribution function from airborne digital holography, Physical review letters, 121, 204 501, 2018.

Lloyd, G., Choularton, T., Bower, K., Crosier, J., Gallagher, M., Flynn, M., Dorsey, J., Liu, D., Taylor, J. W., Schlenczek, O., et al.: Small ice particles at slightly supercooled temperatures in tropical maritime convection, Atmospheric Chemistry and Physics, 20, 3895–3904, 2020.

Lu, J., Shaw, R. A., and Yang, W.: Improved particle size estimation in digital holography via sign matched filtering, Optics Express, 20, 12 666–12 674, 2012.

Meng, H. and Hussain, F.: Holographic particle velocimetry: a 3D measurement technique for vortex interactions, coherent structures and turbulence, Fluid Dynamics Research, 8, 33, 1991.

Meng, H., Anderson, W., Hussain, F., and Liu, D. D.: Intrinsic speckle noise in in-line particle holography, Journal of the Optical Society of America A, 10, 2046–2058, 1993.

Meng, H., Pan, G., Pu, Y., and Woodward, S. H.: Holographic particle image velocimetry: from film to digital recording, Measurement Science and Technology, 15, 673, 2004.

O'Shea, S., Choularton, T., Lloyd, G., Crosier, J., Bower, K., Gallagher, M., Abel, S., Cotton, R., Brown, P., Fugal, J., et al.: Airborne observations of the microphysical structure of two contrasting cirrus clouds, Journal of Geophysical Research: Atmospheres, 121, 13–510, 2016.

Ramelli, F., Beck, A., Henneberger, J., and Lohmann, U.: Using a holographic imager on a tethered balloon system for microphysical observations of boundary layer clouds, Atmospheric Measurement Techniques, 13, 925–939, 2020.

Royer, H.: An application of high-speed microholography: the mertology of fogs, Nouvelle Revue d'Optique, 5, 87, 1974.

Schlenczek, O.: Airborne and ground-based holographic measurement of hydrometeors in liquid-phase, mixed-phase and ice clouds, Ph.D. thesis, University of Mainz, 2018.

Schlenczek, O., Nordsiek, F., Brunner, C. E., Chávez-Medina, V., Thiede, B., Bodenschatz, E., and Bagheri, G.: Airborne measurements of turbulence and cloud microphysics during PaCE 2022 using the Advanced Max Planck CloudKite Instrument (MPCK+), Earth System Science Data Discussions, 2025, 1–29, 2025.

Schröder, M.: Cloud Microphysics Investigations with the Cloudkite Laboratory, Ph.D. thesis, Georg-August-Universität Göttingen Göttingen, 2023.

Shaw, R. A.: Particle-turbulence interactions in atmospheric clouds, Annual Review of Fluid Mechanics, 35, 183–227, 2003.

Spuler, S. M. and Fugal, J.: Design of an in-line, digital holographic imaging system for airborne measurement of clouds, Applied optics, 50, 1405–1412, 2011.

Svizher, A. and Cohen, J.: Holographic particle image velocimetry system for measurements of hairpin vortices in air channel flow, Experiments in fluids, 40, 708–722, 2006.

Tao, B., Katz, J., and Meneveau, C.: Statistical geometry of subgrid-scale stresses determined from holographic particle image velocimetry measurements, Journal of Fluid Mechanics, 457, 35–78, 2002.

Thiede, B., Larsen, M. L., Nordsiek, F., Schlenczek, O., Bodenschatz, E., and Bagheri, G.: Highly Localised Droplet Clustering in Shallow Cumulus Clouds, https://arxiv.org/abs/2502.19272, 2025a.

Thiede, B., Schlenczek, O., Stieger, K., Ecker, A., Bodenschatz, E., and Bagheri, G.: In-line holographic droplet imaging: Accelerated classification with convolutional neural networks and quantitative experimental validation, EGUsphere, 2025, 1–39, 2025b.

Tyler, G. A. and Thompson, B. J.: Fraunhofer holography applied to particle size analysis a reassessment, Optica Acta: International Journal of Optics, 23, 685–700, 1976.

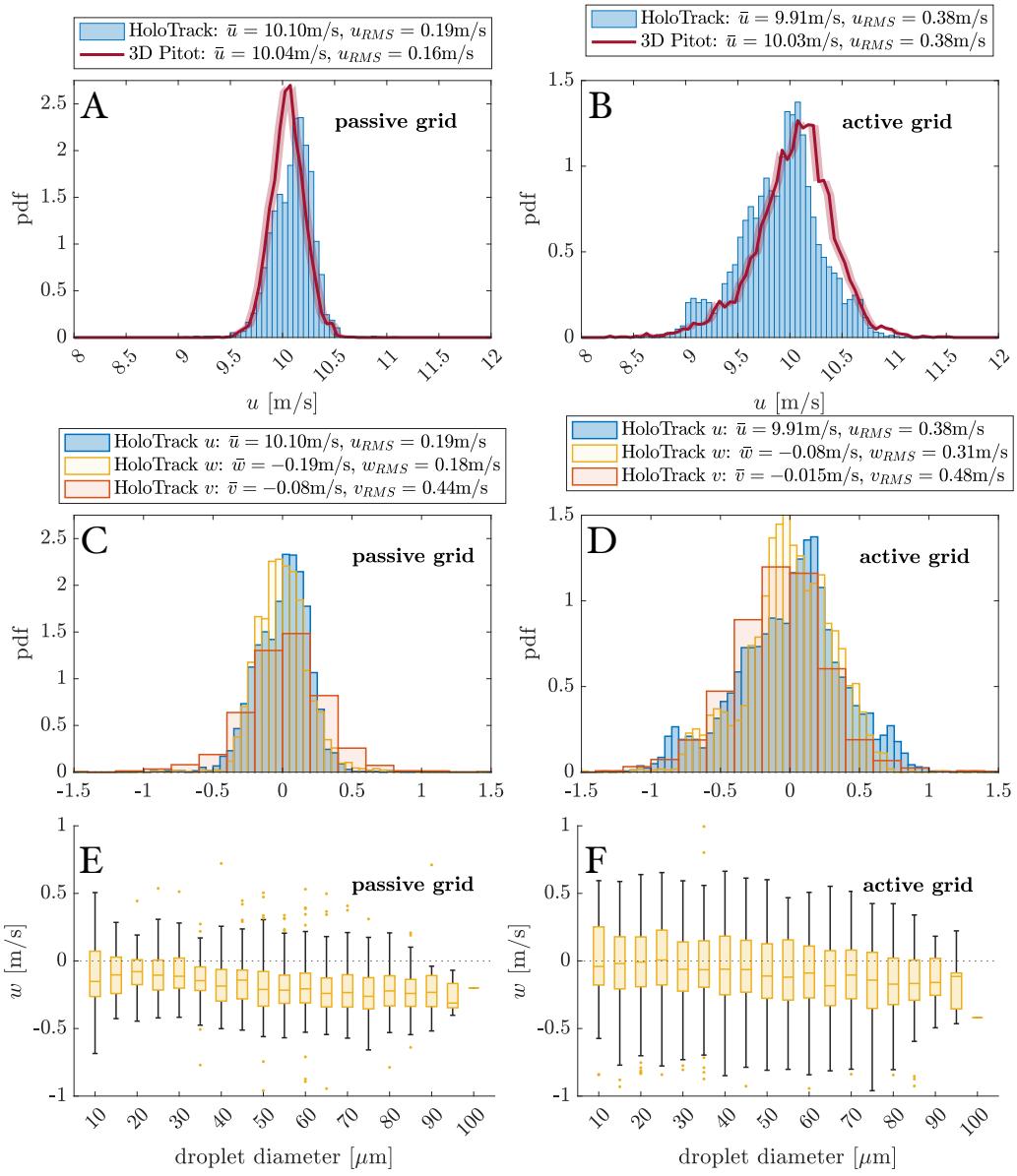


**Figure 13.** Comparison of ~~velocity probability functions from flow measurement with the 3D pitot tube~~ longitudinal 3D-pitot-tube and ~~the droplet~~ holographic (HoloTrack) $u$ velocity measurements for passive (A) and active (B) grid conditions and comparison of velocity fluctuations in all three directions measured with ~~the holographic system. Left: Passive~~ HoloTrack for passive (~~open~~C) and active (D) grid ~~produces lower turbulence intensity that~~ conditions. Accurate measurement of longitudinal component $u$ is ~~close~~ confirmed by comparison to ~~estimated velocity uncertainty~~ 3D-pitot measurement (A,B), while $w_{RMS} \approx u_{RMS}$ in isotropic conditions confirms accurate measurement of ~~HoloTrack~~$w$, $v'$ is biased by high $z$-position uncertainty. ~~Right: pitot~~ Panel E and ~~holographic system measure agree on $TI$~~ F show diameter dependent vertical droplet velocity $w$ to showcase HoloTrack's strength in ~~the more turbulent flow with the active grid~~measuring size and velocity simultaneously.

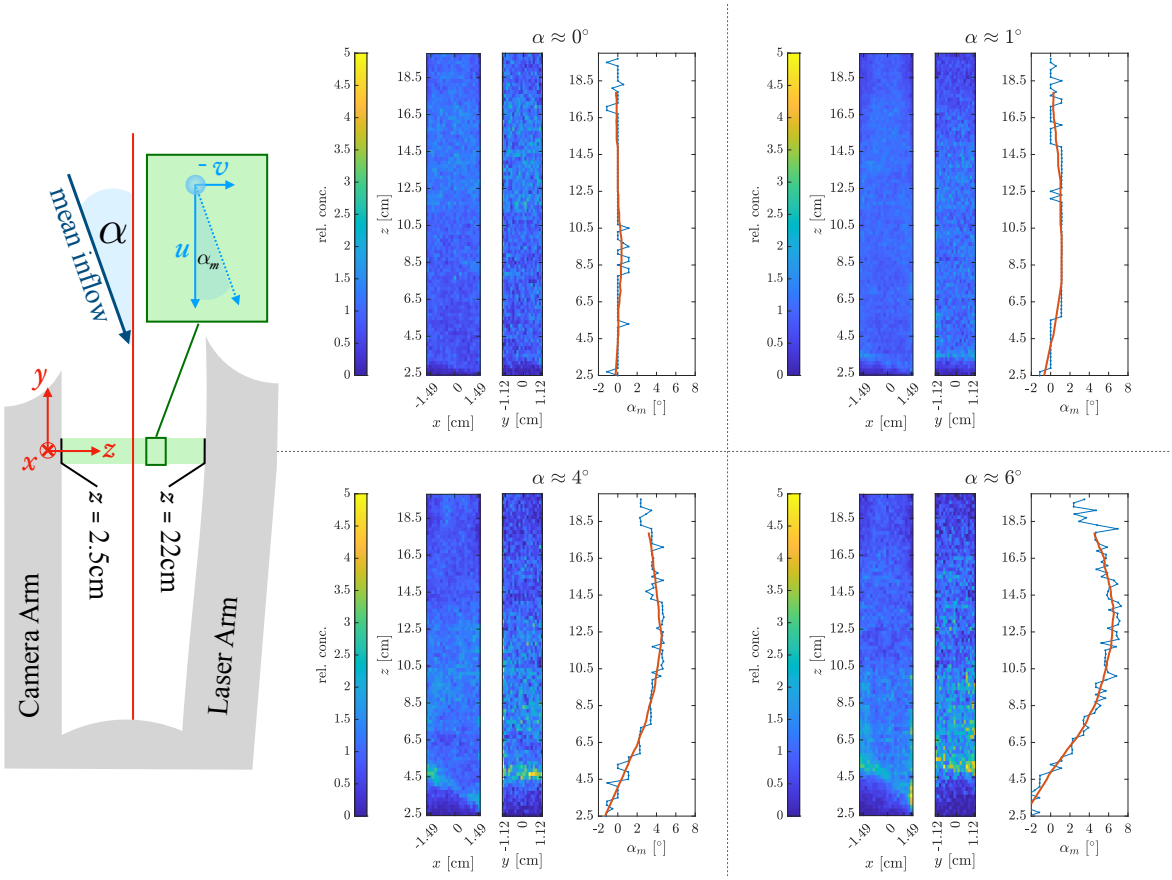


**Figure 14.** If the mean flow has a non-zero yaw angle with respect to HoloTrack's $y$-axis the holographic sample volume is influences by the obstructing arms. The influence can be analyzed with super-holograms revealing void regions and regions of droplet accumulation. The holographic arms also force the flow to align with the direction if the arms, which is revealed by analyzing the $z$-dependence of the droplet velocity direction angles $\alpha_m$ that approaches $0^\circ$ in the vicinity of the arms. If $\alpha \neq 0$, which can reliably measured with the 3D pitot tube, the usable sub-volume of the holographic sample volume needs to be adjusted.